

## Review

**4D Flow MRI****CME**

Michael Markl, PhD,<sup>1,2\*</sup> Alex Frydrychowicz, MD,<sup>3,4</sup> Sebastian Kozerke, PhD,<sup>5</sup>  
Mike Hope, MD,<sup>6</sup> and Oliver Wieben, PhD<sup>3,7,8</sup>

This article is accredited as a journal-based CME activity. If you wish to receive credit for this activity, please refer to the website: [www.wileyblackwellcme.com](http://www.wileyblackwellcme.com)

**ACCREDITATION AND DESIGNATION STATEMENT**

Blackwell Futura Media Services designates this journal-based CME activity for a maximum of 1 *AMA PRA Category 1 Credit*<sup>™</sup>. Physicians should only claim credit commensurate with the extent of their participation in the activity.

Blackwell Futura Media Services is accredited by the Accreditation Council for Continuing Medical Education to provide continuing medical education for physicians.

**EDUCATIONAL OBJECTIVES**

Upon completion of this educational activity, participants will be better able to evaluate currently used 4D flow MRI methods, including Cartesian and radial data acquisition, approaches for accelerated data acquisition, cardiac gating, and respiration control.

**ACTIVITY DISCLOSURES**

No commercial support has been accepted related to the development or publication of this activity.

## Faculty Disclosures:

The following contributors have no conflicts of interest to disclose:

Editor-in-Chief: C. Leon Partain, MD, PhD

CME Editor: Scott B. Reeder, MD, PhD

CME Committee: Scott Nagle, MD, PhD, Pratik Mukherjee, MD, PhD, Shreyas Vasanawala, MD, PhD, Bonnie Joe, MD, PhD, Tim Leiner, MD, PhD, Sabine Weckbach, MD, Frank Korosec, PhD

Authors: Michael Markl, PhD, Alex Frydrychowicz, MD, Sebastian Kozerke, PhD, Mike Hope, MD, Oliver Wieben, PhD

This manuscript underwent peer review in line with the standards of editorial integrity and publication ethics maintained by *Journal of Magnetic Resonance Imaging*. The peer reviewers have no relevant financial relationships. The peer review process for *Journal of Magnetic Resonance Imaging* is double-blinded. As such, the identities of the reviewers are not disclosed in line with the standard accepted practices of medical journal peer review.

Conflicts of interest have been identified and resolved in accordance with Blackwell Futura Media Services's Policy on Activity Disclosure and Conflict of Interest. No relevant financial relationships exist for any individual in control of the content and therefore there were no conflicts to resolve.

**INSTRUCTIONS ON RECEIVING CREDIT**

For information on applicability and acceptance of CME credit for this activity, please consult your professional licensing board.

This activity is designed to be completed within an hour; physicians should claim only those credits that reflect the time actually spent in the activity. To successfully earn credit, participants must complete the activity during the valid credit period.

Follow these steps to earn credit:

- Log on to [www.wileyblackwellcme.com](http://www.wileyblackwellcme.com)
- Read the target audience, educational objectives, and activity disclosures.
- Read the article in print or online format.
- Reflect on the article.
- Access the CME Exam, and choose the best answer to each question.
- Complete the required evaluation component of the activity.

This activity will be available for CME credit for twelve months following its publication date. At that time, it will be reviewed and potentially updated and extended for an additional period.

<sup>1</sup>Department of Radiology, Feinberg School of Medicine, Northwestern University, Chicago, Illinois, USA.

<sup>2</sup>Department of Biomedical Engineering, Northwestern University, Chicago, Illinois, USA.

<sup>3</sup>Department of Radiology, University of Schleswig-Holstein, Campus Lübeck, Germany.

<sup>4</sup>Department of Radiology, University of Wisconsin – Madison, Wisconsin, USA.

<sup>5</sup>Institute for Biomedical Engineering, University and ETH Zurich, Switzerland.

<sup>6</sup>University of California – San Francisco, California, USA.

<sup>7</sup>Department of Medical Physics, University of Wisconsin – Madison, Wisconsin, USA.

<sup>8</sup>Department of Biomechanical Engineering, University of Wisconsin – Madison, Wisconsin, USA.

Contract grant sponsor: Bundesministerium für Bildung und Forschung (BMBF); Contract grant number: 01EV0706; Contract grant sponsor: NMH Excellence in Academic Medicine (EAM) Program, "Advanced Cardiovascular MRI Research Center".

Traditionally, magnetic resonance imaging (MRI) of flow using phase contrast (PC) methods is accomplished using methods that resolve single-directional flow in two spatial dimensions (2D) of an individual slice. More recently, three-dimensional (3D) spatial encoding combined with three-directional velocity-encoded phase contrast MRI (here termed 4D flow MRI) has drawn increased attention. 4D flow MRI offers the ability to measure and to visualize the temporal evolution of complex blood flow patterns within an acquired 3D volume. Various methodological improvements permit the acquisition of 4D flow MRI data encompassing individual vascular structures and entire vascular territories such as the heart, the adjacent aorta, the carotid arteries, abdominal, or peripheral vessels within reasonable scan times. To subsequently analyze the flow data by quantitative means and visualization of complex, three-directional blood flow patterns, various tools have been proposed. This review intends to introduce currently used 4D flow MRI methods, including Cartesian and radial data acquisition, approaches for accelerated data acquisition, cardiac gating, and respiration control. Based on these developments, an overview is provided over the potential this new imaging technique has in different parts of the body from the head to the peripheral arteries.

**Key Words:** 4D flow MRI; blood flow; phase contrast; respiration control; PC-VIPR; self-gating; intracranial arteries; carotid bifurcation; aorta; pulmonary arteries; heart; hepatic arteries; renal arteries; peripheral arteries; hemodynamics

**J. Magn. Reson. Imaging 2012;36:1015–1036.**

© 2012 Wiley Periodicals, Inc.

CARDIOVASCULAR MAGNETIC RESONANCE IMAGING (MRI) has undergone substantial developments over the last decades and offers capabilities for evaluating cardiac anatomy and function including cardiac viability, perfusion, blood flow, and vascular anatomy.

Phase contrast (PC) MRI can be used to measure and quantify pulsatile blood flow in the human vascular system. The basic principle was introduced by Carr and Purcell in 1954 (1), who reported the first observation of coherent motion on the MR-signal, and by Hahn in 1960 (2), who applied flow-sensitive MRI to detect seawater motion. The first in vivo velocity map images and applications were reported in the early 1980s (3–6). Since then, two-dimensional (2D) and time-resolved (electrocardiogram [ECG]-gated “CINE” imaging) PC MRI has become available on all modern MR systems and is an integral part of clinical protocols assessing blood flow and cardiac and valve function in the heart and large vessels (7,8).

Recent developments permit the comprehensive acquisition and analysis of blood flow dynamics with full volumetric coverage of the vascular territory of interest (9–12). By doing so, a posteriori analyses of hemody-

namics have become possible. The term “4D flow MRI” used in this review article refers to three-dimensional (3D) data acquired in a time-resolved, ECG-gated, manner with velocity encoding in all three spatial directions.

3D visualization can be performed in order to depict the configuration and changes of blood flow patterns based on the acquired velocity vectors in all three spatial dimensions (13–19). Retrospective quantification enables a comprehensive analysis of regional cardiac and vascular hemodynamics (20–23). In addition to the measurements of basic flow volumes and velocities, the estimation of derived hemodynamic biomarkers such as wall shear forces (24–26), pulse wave velocity (27,28), pressure gradients (29–31), and other measures (32,33) have been proposed.

The purpose of the review is to introduce the reader to currently available acquisition and analysis methods for 4D flow MR imaging. We will also provide an overview over potential clinical applications in various vascular regions throughout the body that have been reported.

## METHODS

### *Phase Contrast MRI: Basic Principle and Standard Techniques*

The intrinsic sensitivity of MRI toward motion can be used with PC MRI to image vessel anatomy for PC MR angiography (34) but also to directly measure blood flow velocities. The underlying concept of velocity encoding is based on the observation that changes in the MR signal phase along a magnetic field gradient are directly related to the blood flow velocity. Using appropriate bipolar velocity encoding gradients, flow-dependent phase changes can be detected by playing out two acquisitions with different velocity-dependent signal phase but otherwise identical sequence parameters (7,8,35). Subtraction of the two resulting phase images (ie, calculation of phase difference images  $\Delta\phi$ ) allows for the removal of the unknown background phase and calculation of velocity images. This approach is generally referred to as PC MRI, flow-sensitive MRI, or MR velocity mapping.

Standard MR acquisitions are too slow to capture dynamics within the cardiac cycle in real time with sufficient spatial resolution. Instead, the acquisition is split over multiple heartbeats and data acquisition has to be gated to the cardiac cycle using the ECG signal (eg, the R-wave) or a pulse oximeter reading. A series of time-resolved (CINE) images is collected representing the dynamics of the pulsatile blood flow during the cardiac cycle (7,36,37).

Standard techniques use PC MRI methods that provide velocity maps with two spatial dimensions (2D) on individually placed imaging slices. Usually, one-

\*Address reprint requests to: M.M., Departments of Radiology and Biomedical Engineering, Northwestern University Feinberg School of Medicine, 737 N. Michigan Ave. Suite 1600, Chicago, IL 60611. E-mail: mmarkl@northwestern.edu

Received August 15, 2011; Accepted February 6, 2012.

DOI 10.1002/jmri.23632

View this article online at [wileyonlinelibrary.com](http://wileyonlinelibrary.com).

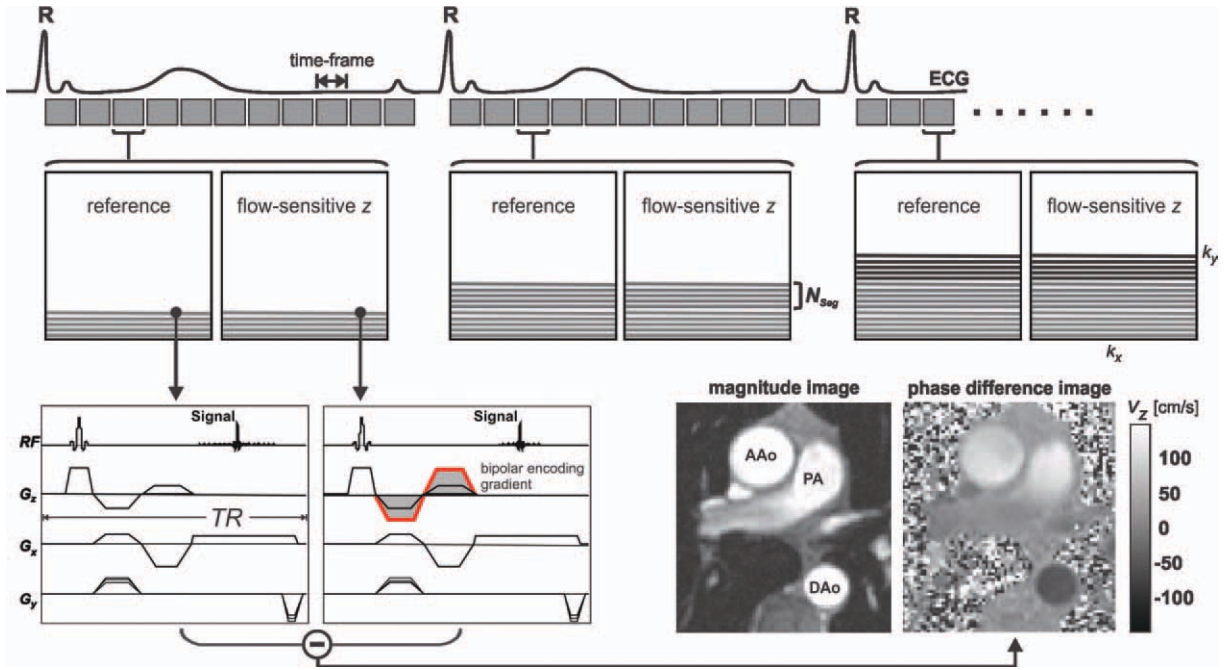


**Figure 1.** Standard 2D CINE PC MRI with one-directional through-plane ( $z$ ) velocity encoding. Reference and velocity sensitive scan (added bipolar encoding gradient) are acquired in direct succession. The subtraction of both datasets provides phase difference images that contain quantitative blood flow velocities as shown in a 2D slice normal to the ascending (AAo) and descending (DAo) aorta and including the pulmonary artery (PA). Due to time constraints, the MR data cannot be acquired during a single heartbeat and PC data are collected over several cardiac cycles. The measurement is synchronized with the cardiac cycle using an ECG-gated  $k$ -space segmented data acquisition. For each heartbeat and time frame only a subset ( $N_{Seg}$ ) of all required ( $N_y$ ) phase-encoding steps are measured ( $k$ -space segmentation). The procedure is repeated until the full raw dataset is acquired and time-resolved (CINE) images can be derived depicting the dynamics of pulsatile through plane flow. The selection of the number of phase-encoding lines  $N_{Seg}$  determines the temporal resolution (time to collect data for a single time frame  $\Delta t = 2 TR N_{Seg}$ ) and a total scan time  $T_{acq} = N_y / N_{Seg} T_{CC}$  of the phase contrast CINE acquisition ( $T_{CC}$  = duration of one cardiac cycle). For a typical TR on the order of 5–10 msec and  $N_{Seg} = 3$ –4, measurements can be performed during breath-holding and with temporal resolutions of 30–80 msec. Typical velocity sensitivities are  $V_{enc} = 150$  cm/s for aortic flow measurements and  $V_{enc} = 100$  cm/s for flow in the pulmonary artery. The presence of stenosis will require selection of higher velocity sensitivities for properly capturing accelerated flow. [Color figure can be viewed in the online issue, which is available at [wileyonlinelibrary.com](http://wileyonlinelibrary.com).]

directional (“through plane”) velocity encoding along the predominant blood flow direction is used to quantify blood flow in the heart, through cardiac valves, and in great vessels. A typical data acquisition strategy for standard 2D CINE PC MRI, which can be performed during a single breath hold, is illustrated in Fig. 1 (for details on typical imaging parameters see figure legend).

It is important to note that PC MRI requires the user to define an upper velocity limit, the velocity sensitivity encoding parameter  $V_{enc}$ .  $V_{enc}$  is defined as the (positive or negative) maximum velocity that can be detected without error. For velocities exceeding the  $V_{enc}$ , velocity aliasing occurs. In this case, the acquisition needs to be repeated with an increased  $V_{enc}$  or antialiasing correction needs to be performed to achieve data that can be properly quantified. PC MRI thus requires prior knowledge (approximation) of the maximum velocities that are expected in the vessel of interest. The  $V_{enc}$  can be flexibly adjusted by the user. Changes in  $V_{enc}$  correspond to changing the strengths and duration of the velocity encoding gradients, where the encoding of lower velocities requires larger gradi-

ent areas and thus longer echo and repetition times (TE and TR).

As for all MR images, the quality of PC velocity images can be degraded by noise. The velocity noise in PC MRI is directly proportional to the  $V_{enc}$  and inversely related to the signal-to-noise ratio (SNR) in the corresponding magnitude images, ie,  $v_{noise} \approx V_{enc} / \text{SNR}$  (7). Hence, both properties of PC-MRI, high  $V_{enc}$  to avoid aliasing and low  $V_{enc}$  to reduce noise, need to be considered for the selection of the optimal velocity sensitivity. In essence, the user should choose the highest expected velocity to avoid unintentional wrapping in the velocity images and check the resulting image before the patient leaves the scanner. At the same time keeping the  $V_{enc}$  as low as possible will reduce velocity noise and improve image quality.

#### 4D Flow MRI: Data Acquisition

Full 3D CINE coverage with three-directional velocity encoding, ie, “4D flow MRI,” can be achieved using standard Cartesian or technically more demanding radial image acquisition. Since the acquisition of

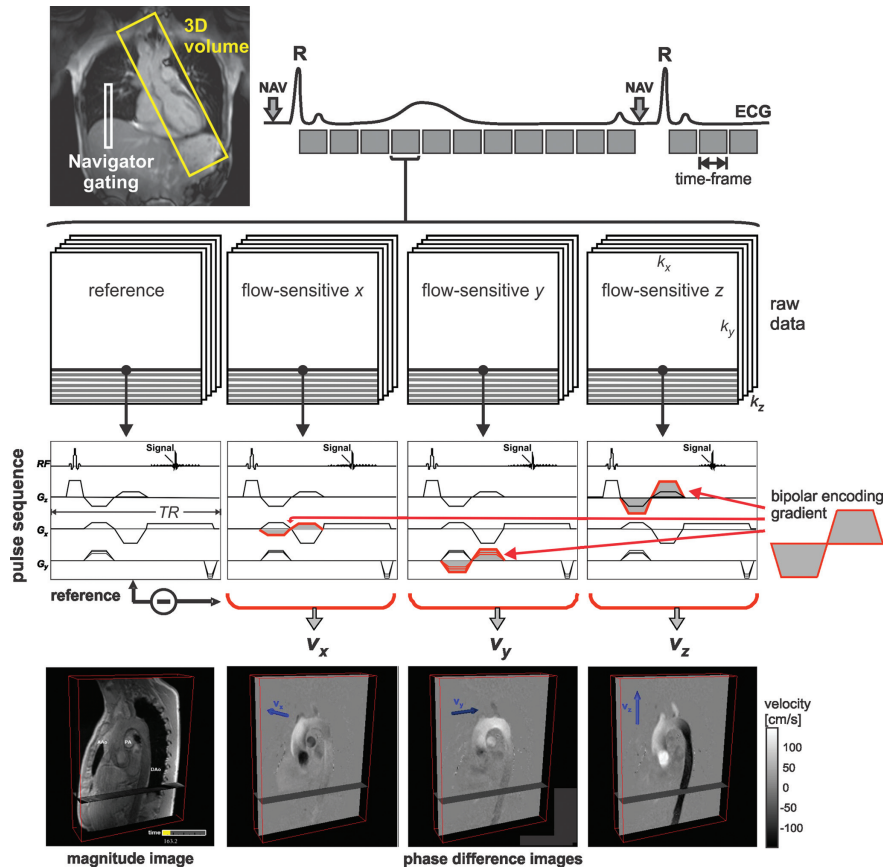


**Figure 2.** Schematic illustration of Cartesian 4D flow MRI of the thoracic aorta. For each time frame, four 3D raw datasets are collected to measure three-directional blood flow velocities ( $v_x$ ,  $v_y$ ,  $v_z$ ) with a reference scan and three velocity-encoded acquisitions. Navigator gating of the diaphragm motion can be used for image acquisition during free breathing. The navigator pulse (NAV) is played out at the end of each cardiac cycle to update the current respiration phase which is used for respiratory gating.  $K$ -space segmentation is used to collect a subset ( $N_{Seg}$ ) of all required ( $N_y N_z$ ) phase-encoding steps for each time frame. The selection of  $N_{Seg}$  determines the temporal resolution  $\Delta t = 4 TR N_{Seg}$  and total scan time  $T_{acq} = N_y N_z / N_{Seg} T_{ECG}$ . For applications in the aorta or pulmonary systems a typical TR on the order of 5–6 msec, spatial resolution  $\approx 2 \times 2 \times 2 \text{ mm}^3$ ,  $V_{enc} = 100\text{--}150 \text{ msec}$ ,  $N_{Seg} = 2$ , parallel imaging with  $R = 2$ , navigator efficiency = 50%–80% results in a total scan time of approximately 15–20 minutes with a temporal resolution of 40–50 msec.

volumetric data requires considerably longer total scan times (up to 20 minutes) compared with traditional 2D-CINE-PC, exams can no longer be performed during a breath hold. Therefore, different strategies to incorporate respiration control have to be considered for thoracic and abdominal 4D flow MRI.

#### Cartesian 4D Flow MRI and Three-Directional Velocity Encoding

The need to collect time-resolved volumetric data combined with three-directional velocity encoding requires an efficient data acquisition to reduce the scan time to clinically feasible durations.  $K$ -space segmentation and interleaved four-point velocity encoding are used to acquire 3D CINE data in combination with respiratory gating, as illustrated in Fig. 2. As in 2D CINE PC MRI, measurements are based on radiofrequency (RF)-spoiled gradient echo sequences with short TE and TR times. During each cardiac cycle, a subset ( $N_{Seg}$ ) of all required phase-encoding steps ( $N_y N_z$   $k$ -space lines along phase ( $k_y$ ) and slice ( $k_z$ ) encoding

direction) is collected. The procedure is repeated for a total of  $N_y N_z / N_{Seg}$  heartbeats to achieve full 3D volumetric coverage (11,38).

Multiple approaches have been used to perform three-directional flow encoding. The earliest approach was following the logic that for each encoded velocity direction a pair of measurements is required. Similar to one-directional velocity encoding in Fig. 1, one flow-compensated and one flow-encoded measurement per direction resulted in a time-intensive technique that was referred to as a “six-point method” (34). Later, and as currently used for 4D flow techniques, more time-efficient “four-point” techniques were introduced. As illustrated in Fig. 2, for each single raw data ( $k$ -space) line four successive acquisitions are collected to achieve velocity encoding in all three dimensions: one reference scan and the three velocity-encoded acquisitions (added bipolar gradients along  $x$ -,  $y$ -,  $z$ -direction). After the data acquisition is completed, image reconstruction yields 3D CINE magnitude data (anatomical images) and three time series representing the three-directional blood flow velocities

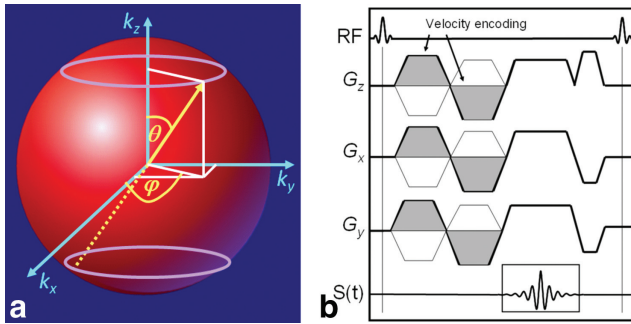


**Figure 3.** In 3D radial acquisitions, every acquired  $k$ -space line traverses through the center of  $k$ -space (a). The endpoints of the projections cover the surface of a sphere so that the resulting imaging volume is a sphere also. With radial undersampling, scan time is reduced at the expense of streak-like artifacts and a reduced SNR while spatial resolution is preserved. As shown in the pulse sequence diagram (b), there is no traditional readout gradient, phase-encoding gradient, and slice-encoding gradient in a radial acquisition. The gradient waveforms are scaled with the azimuthal and inclination angle of the projection and bipolar gradient pairs are added for velocity-encoded scans such as PC VIPR.

$v_x$ ,  $v_y$ , and  $v_z$  (phase difference images). Interleaved velocity encoding, which requires the successive acquisition of the same phase-encoding line with four different velocity-encoding gradients, results in a lower limit for the temporal resolution of  $\Delta t = 4$  TR. The selection of the  $V_{enc}$  will impose requirements on the area under of the bipolar velocity-encoding gradients and thus influence the minimum achievable echo and repetition times TE and TR. For typical cardiovascular applications with a  $V_{enc}$  ranging between 50–200 cm/sec, the TE and TR can be as low as 2–4 msec and 5–7 msec.

In addition to the “simple” (or “referenced”) four-point method using a single reference scan and a series of three velocity-encoded scans as shown in Fig. 2, other “balanced” four-point methods have been proposed. For a more detailed description, please refer to Pelc et al (39), Bernstein et al (35), and Johnson and Markl (40).

#### Radial 4D Flow MRI (PC-VIPR)

Scan times for 4D flow MRI can become prohibitively long, especially when high spatial resolution or large volumetric coverage are preferable. Several methods have been proposed for reductions in scan time including the use of parallel imaging (41) and sampling strategies that explore correlations in the spatio-temporal domain (42) or both (43).

A promising approach for accelerated PC MRI is the use of radial undersampling. With this approach, data points in  $k$ -space are recorded on a radial trajectory as shown in Fig. 3. In a 3D radial acquisition, each recorded data line passes through the center of  $k$ -space. The resolution along the rotating readout direction remains constant for each projection angle and provides an isotropic spatial resolution over a spheri-

cal imaging volume. In contrast to traditional Cartesian sampling with parallel lines in  $k$ -space, spatial resolution is preserved even if fewer radial lines are acquired than dictated by the Nyquist limit (44). Instead of a compromised resolution, the tradeoffs for scan time reductions are streak artifacts and a loss of SNR.

It has been shown that PC MRI acquisitions are well suited for radial undersampling due to the inherent subtraction of signal from static tissues (45). Moderate streak artifacts can be tolerated in these images that are characterized by high contrast and sparse signal distribution from the vessels. A 3D radial flow sensitive acquisition, introduced as PC VIPR (vastly undersampled isotropic projection reconstruction) (46), provides coverage of a large imaging volume with high spatial resolution in all three dimensions. Additional scan time savings can be achieved for cardiac gated acquisitions by temporal filtering (47), which offers greater flexibility for “view sharing” of radial data compared with Cartesian datasets. Non-Cartesian trajectories are more sensitive to several artifacts and the method was refined to minimize trajectory errors, off-resonance effects, and aliasing artifacts from undersampling (48).

Advantages of PC VIPR acquisitions include: 1) isotropic spatial resolution for image reformatting in oblique planes and improved hemodynamic analysis; 2) large volume coverage; and 3) high spatial resolution, which also reduces partial volume effects and intravoxel dephasing. Radial sampling has also been shown to offer several advantages in dealing with motion: i) the appearance of motion artifacts is generally reduced (49); ii) self gating to the cardiac (50) and respiratory cycle (51) is possible of the radial signal itself; and iii) retrospective cardiac gating is facilitated.

PC VIPR has been shown to generate high-quality MR angiograms for vessels of various sizes without a contrast agent (52). It has also been used for hemodynamic analysis in applications that demand high spatial resolution, such as cranial aneurysms (53) and measurements of trans-stenotic pressure gradients (54–56); or large volumetric coverage as often needed on congenital heart disease (57); or both including cranial imaging (58) and imaging of the hepatic and portal venous system (59).

#### Respiration Control

For thoracic and abdominal applications, patient breathing can cause data inconsistencies that result in image ghosting and blurring. Therefore, respiratory gating is usually applied to minimize artifacts. Most widely available approaches include bellows reading or navigator gating (60–63). In both, a range or window of accepted and rejected diaphragm positions can be defined. In the case of bellows reading, the excursion of the upper abdominal circumference serves as the indirect indicator of the diaphragm position and hence breathing motion. Similarly, navigator gating can be used to regularly (eg, for each cardiac cycle) provide information on the diaphragm position during

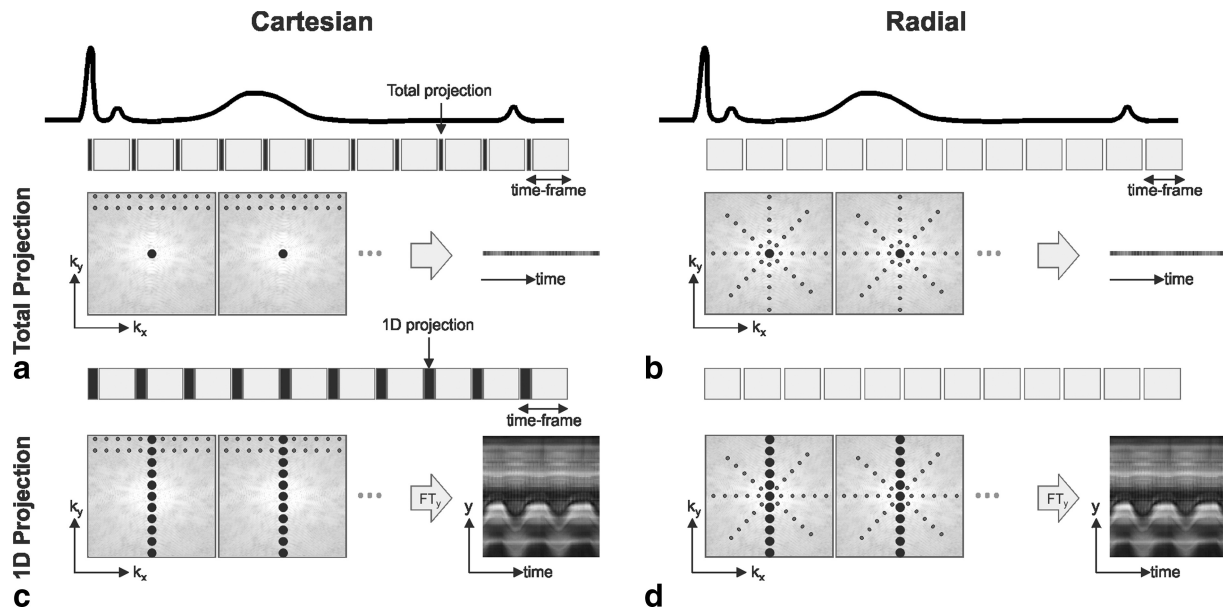


**Figure 4.** Self-gating principle for Cartesian and radial imaging. Using the total projection concept the central  $k$ -space point is repetitively measured for each time-frame. Since the central  $k$ -space point reflects the integral of the object signal within the sensitive volume, motion leads to a modulation of  $k$ -space signal, which can be directly used for respiratory gating (**a,b**). In order to add spatial resolution, entire  $k$ -space profiles may be imaged such that, upon Fourier transform, spatial resolution along a main component of motion is obtained (**c,d**). While sequence modification is necessary to repetitively sample the  $k$ -space center or a specific profile in Cartesian imaging, which also prolongs TR and/or the duration of a time-frame (**a,c**), radial scanning inherently samples the  $k$ -space center or profiles suitable for self-gating and hence sequence timing remains unchanged (**b,d**).

the 4D flow MRI data acquisition. For respiratory gating, data are accepted if the current breathing position is within a predefined end-expiratory or end-inspiratory window. Otherwise, data collected during the current cardiac cycle are rejected and the acquisition is repeated until the gating criteria have been met. A certain amount of data, typically 40%–60%, is thus rejected thereby prolonging the total exam time compared with nonrespiratory-gated 4D flow MRI acquisitions. Adaptive  $k$ -space reordering, ie, phase encoding based on the current position in the respiration cycle, can reduce data rejection to 20%–40% (38,64,65).

#### Advanced Physiological Control

While navigator gating based on 1D measurements of diaphragm motion has been widely adopted for 4D flow measurements by most vendors, it has two drawbacks. First, detection of motion of the organ of interest is typically based on measurements of remote anatomy. For example, in cardiac imaging respiratory-induced motion of the heart is typically inferred from measurements of displacement of the lung–liver interface (60). It has been demonstrated that the relation between heart and liver motion may be offset and, consequently, correction factors to account for deformation (66) and respiratory hysteresis (67) have been proposed. A second drawback relates to the time it takes to acquire navigator data, which only permits a single or two navigators per cardiac cycle in most situations. It has been shown that this low temporal update can lead to a poor prediction of respiratory

motion for the cardiac phases acquired long after a navigator signal (63).

In addressing these shortcomings, respiratory self-gating methods have been proposed (50,68,69) that repetitively acquire  $k$ -space data of the object itself to provide information of object motion (Fig. 4). Self-gating methods re-visit the central  $k$ -space point or specific profiles in each time-frame of the cardiac cycle, and hence sample respiratory induced signal fluctuation at a high temporal rate. Sampling the central  $k$ -space point provides the integral of the entire object signal within the sensitive imaging volume. Accordingly, the amplitude is modulated as the object moves relative to the receive antennae used.

Such an approach adds only little time to each time-frame in Cartesian imaging but it may be compromised in patients with significant body fat, as the bright fat signal may mask motion-induced signal changes of the object of interest. Accordingly, self-gating methods have been extended to measure entire profiles oriented such that major components of motion are captured with 1D projections (51,70). In Cartesian cine imaging this, however, leads to a reduction of the number of time-frames that can be acquired during a cardiac cycle, as one additional TR is required per time-frame to measure projections. While the additional sampling of a single  $k$ -space point or entire profiles in Cartesian imaging prolongs the duration of each time-frame, radial imaging methods offer an elegant approach to inherently acquire motion-related information without time penalty (51). In combination with PC-VIPR and related Golden angle radial imaging techniques (71), these self-gating

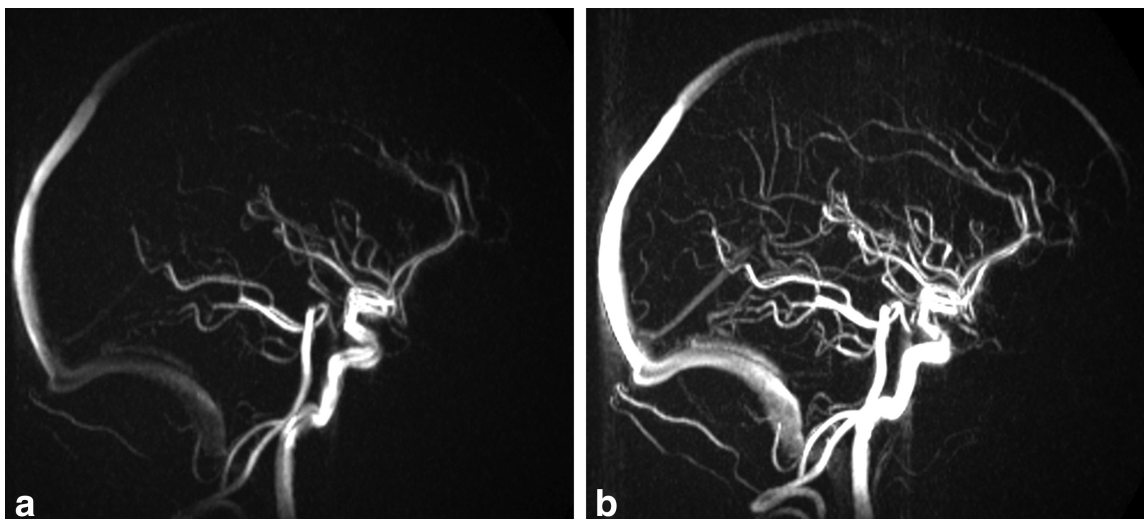


**Figure 5.** PC-MRA of a 5-minute cranial PC VIPR scan acquired with a  $V_{enc}$  of 80 cm/s (**a**) and 25 cm/s (**b**). A 3D PC-MRA is derived from combining the magnitude and velocity data, most commonly achieved by complex difference processing. The resulting angiogram suppresses signal from nonmoving tissue and shows the vessel lumens of arteries and veins. These angiograms can be used for vessel segmentation and processing of the velocity data and to provide an alternative to MR angiography approaches that rely on the injection of a contrast bolus. A lower  $V_{enc}$  setting (**b**) provides higher SNR and better visualization of vessels with slower blood flows such as veins and smaller arteries.

approaches seem most promising to provide motion information for respiratory gating purposes.

As respiratory gating leads to partial rejection of data acquired during rapid motion, overall scan efficiency is typically reduced by 20%–60% leading to long overall measurement times in 4D flow imaging. Advanced retrospective motion correction techniques have been developed that permit correction of the acquired data given an estimate of the underlying motion (72). Motion estimates may be obtained from simultaneous recordings from respiratory belts, self-gating signals, or navigators (73). While most self-gating and advanced motion correction methods have been applied to cine imaging, their application to 4D flow imaging remains to be accomplished.

#### **4D Flow MRI: Data Postprocessing and Analysis**

Several sources of error such as background phase contributions from eddy-currents or method-specific problems such as velocity aliasing and noise can compromise MR velocity maps and need to be addressed prior to data processing or visualization. The major sources of errors include eddy current effects, Maxwell terms, and gradient field distortions. Appropriate correction strategies have been presented and validated in the literature and should be applied to ensure accurate 3D visualization and flow quantification using 4D flow MRI data. More details regarding appropriate correction strategies can be found in Walker et al (eddy currents) (74), Bernstein et al (Maxwell terms) (75), and Markl et al (gradient field nonlinearity) (76).

The complex nature of the 4D flow MRI data (three spatial dimensions, three velocity directions, and time within the cardiac cycles) imposes the challenge to

translate the multidimensional information into images that can clearly depict the underlying anatomic and functional information. The combination of angiographic data (3D PC-MRA) and 3D blood flow visualization, which can both be derived from the 4D flow data, can be powerful tools to efficiently display vascular anatomy and blood flow in 3D and over time (see, eg, Figs. 6, 7) (14).

#### *PC-MR Angiography*

Phase contrast imaging has been used to generate MR angiograms (PC MRAs) since the early days of clinical MRI (34). Interest in diagnostic PC MRA was recently renewed by discovering a link between nephrogenic systemic fibrosis (NSF) and gadolinium-based MRA contrast agents (77) as well as the greatly improved 4D flow MRI acquisitions. In addition, the hemodynamic visualization and analysis of 4D flow MRI data greatly benefits from the availability of a detailed angiogram, specifically for proper segmentation of vessels.

There are several strategies for calculating angiograms from acquisitions with three-directional velocity encoding. In general, the velocity and magnitude data are combined to isolate regions with blood flow (ie, high absolute velocities) from surrounding static tissue. The most common approach is the use of complex difference (CD) reconstruction (34,78). With one-directional velocity encoding, a CD image is derived as a complex subtraction of the velocity encoded and the reference scan on a pixel-by-pixel basis. The CD image represents the magnitude of this difference vector. Any directional velocity information is lost in the CD image and it can no longer be used to quantify velocities, but arteries and veins are well differentiated from static background tissues, as shown in Fig. 5. With three-directional velocity encoding, CD

images are calculated for each encoding direction and the final CD image, also referred to as the “speed image,” is derived as the square root of the sum of squares of the three CD images or volumes. Additional examples of PC MRAs are shown in Fig. 12.

The quality of the vessel depiction is strongly influenced by the choice of the velocity sensitivity,  $V_{\text{enc}}$ . Particularly small vessels with slow flow are better depicted using a smaller  $V_{\text{enc}}$ , as shown in Fig. 5b. However, larger vessels with higher blood flow velocities can suffer from decreased signal due to aliasing of the signal phase in low- $V_{\text{enc}}$  scans. For increased  $V_{\text{enc}}$ -factors the visualization of larger arterial vessels is improved and venous signal deteriorates with increased noise. The quality of the depicted vessels is best if the chosen flow sensitivity represents the physiological situation of the vessel segment of interest. However, there is no single optimal  $V_{\text{enc}}$  when a large imaging volume with various vessels is covered.

### 3D Blood Flow Visualization

There are several visualization options of the acquired velocity field that have previously been described in the literature (13–18,79–81). The most basic visualization option is the vector graph display of the acquired data (Fig. 6a). Intuitively, the *vector graph* displays the magnitude and direction of blood velocity within a specific voxel encompassing all three measured velocity directions. Variables such as the acquired velocity can be further encoded by, eg, the individual vector's width or color. The term *streamline* is usually used to describe an instantaneous path tangent to the velocity vectors at a specific point in time (Fig. 6b). Therefore, streamlines are typically not used to represent the periodic time-varying information of the measured flow data but provide an overview over flow field patterns at a specific point within the cardiac cycle. Some software applications allow for a temporal animation of streamlines resulting in animations that can be misleading if the reader is not fully aware of the details of the visualization method. Principally, a streamline can be imagined as the path a massless particle would take in a temporally constant flow field, which is, however, rarely ever the case. For nonstationary pulsatile flow, a representation of the actual path over time is achieved using *time-resolved 3D particle traces* or *pathlines* (Fig. 6c). Such particle traces can be considered massless particles that are emitted at user-defined points (regions, planes, or volumes) within the acquired data volume and follow the flow field over time. It is an intuitive way to display the temporal evolution of the blood flow velocity data over one or multiple heartbeats. Color-coding can be added, eg, to add velocity information or to represent the origin of flow, eg, when emitters are placed in vessel supplying other structures (so-called connectivity mapping) (82).

### Retrospective Quantification

Since 4D flow MRI data reflect the true underlying time-resolved blood flow velocity vector field, it is possible to perform quantitative analysis of the measured

blood flow. A benefit compared with traditional 2D PC-MRI is illustrated in Fig. 7. Based on a 4D flow MRI acquisition and visualization of blood flow it is possible to interactively quantify blood flow velocities and volumes at user selected locations of interest within the 3D volume a posteriori (20–22). Assuming complete coverage of the vascular territory of interest (eg, the entire thoracic aorta in Fig. 7), flow quantification can be carried out in analysis planes at any location along the vessel. Errors due to misalignment of the analysis plane which may occur with traditional 2D PC MRI can thus be minimized. Moreover, scan prescription is relatively simple (positioning of one 3D volume) compared with the necessity to place multiple 2D PC MRI exams at double oblique scan planes associated with the possibility to miss flow information due to an insufficient number or placement of 2D slices. Recent studies have shown excellent agreement between standard 2D CINE PC and 4D flow MRI for quantitative blood flow measurements. Moreover, good test-retest reproducibility and low inter- and intraobserver variability for applications in the aorta and carotid arteries was demonstrated (23,83,84).

In addition to the calculation of regional flow parameters such as peak velocity, time-to-peak flow, total flow, retrograde flow, etc., more advanced quantification methods and algorithms have been presented in the literature. A number of groups have reported techniques to derive additional hemodynamic parameters such as wall shear stress, pulse wave velocity, pressure difference, or turbulent kinetic energy, among others. (20,27–33,55,85,86). A detailed discussion of these methods is beyond the scope of this review article. The application of such data analysis strategies to various vascular diseases will be briefly discussed in the applications section where relevant.

## APPLICATIONS

Over the past two decades a number of groups have reported on the application of 4D flow MRI for the assessment of arterial and venous hemodynamics in various anatomic regions in the human body. Initiated by early work of Kilner et al (16,81), Firmin et al (9), Bogren et al (10,13), Buonocore (14), Wigstrom et al (11,15), and others, 4D flow MRI acquisition techniques and data analysis strategies have continuously evolved. Improvement in MR hardware, more powerful computers, and MR methodology developments such as sparse sampling and parallel imaging have helped to make data acquisition faster and image analysis more clinically feasible (18,48,70,87).

The following sections review various applications of 4D flow MRI to illustrate the potential of this relatively young but promising method to provide comprehensive information on normal and pathologically altered hemodynamics in different anatomical regions. It is neither intended to provide a complete overview over all possible uses of 4D flow MRI nor should the application of 4D flow MRI be restricted to the presented applications. Instead, the authors believe that most presented principles can be easily transferred to most vascular

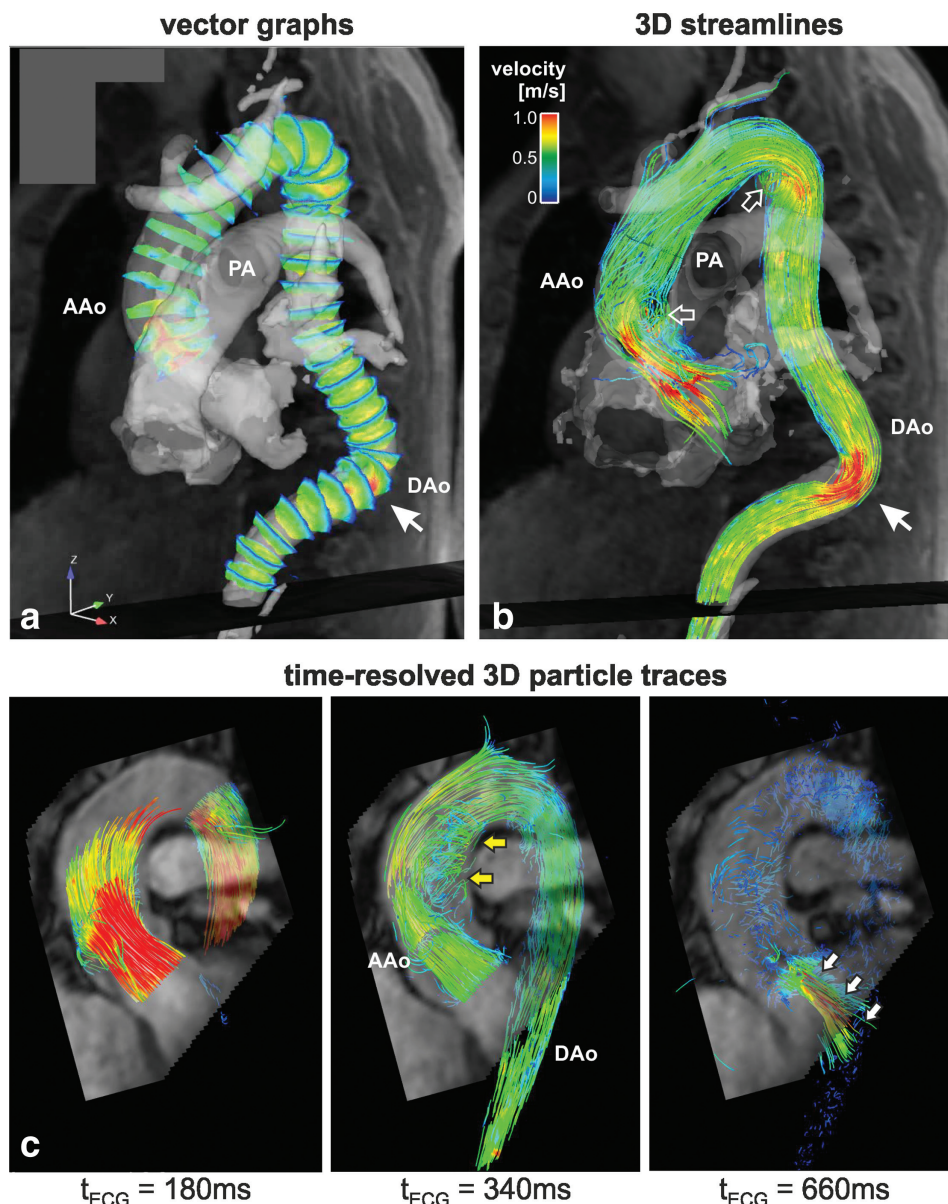


**Figure 6.** 3D blood flow visualization in the thoracic aorta in a patient with an unusually complex aortic shape including kinking and elongation of the descending aorta (A,B) and a patient with aortic valve insufficiency (C). For A,B, 3D PC-MRA data (gray shaded, semitransparent isosurface) was used to depict aortic vessel anatomy and aid 3D visualization. **a:** Vector graphs visualize flow profiles in multiple analysis planes along the aorta. The length of the vector and the color of the vector both represent the local velocity. **b:** 3D streamlines permit the visualization of the 3D distribution of systolic velocities in the entire aorta. The images illustrate the impact of the complex aortic shape on blood flow such as the physiologically expected acceleration of flow at bends (eg, solid arrow) but also vortical flow patterns in the ascending and proximal descending aorta (open arrows). **c:** Time-resolved 3D pathlines during systole and diastole in a patient with aortic valve insufficiency illustrate spatiotemporal dynamics of blood flow including systolic helix formation in the ascending aorta (yellow arrows) and the formation of a diastolic retrograde flow jet (white arrows). Color coding = local absolute blood flow velocity. AAo, ascending aorta; DAo, descending aorta; PA, pulmonary artery.

regions. A summary of typical imaging parameters for different anatomic regions is provided in Table 1.

### Heart and Great Vessels

#### Aortic Hemodynamics

Evaluation of dynamic blood flow in the thoracic aorta with PC MRI has been a topic of considerable interest for over 20 years. The aorta is a vessel of great clinical

importance and its large size eases the demands on spatial resolution for proper flow characterization. Beginning in the late 1980s, normal blood flow in the thoracic aorta was studied in detail throughout the cardiac cycle (13,81,88). Synthesizing observations from 2D imaging planes acquired from multiple volunteers, Kilner et al (81) were able to illustrate “typical” flow patterns including a right-handed twist to flow in the ascending aorta during late systole and retrograde flow streams during diastole. With the advent of 3D

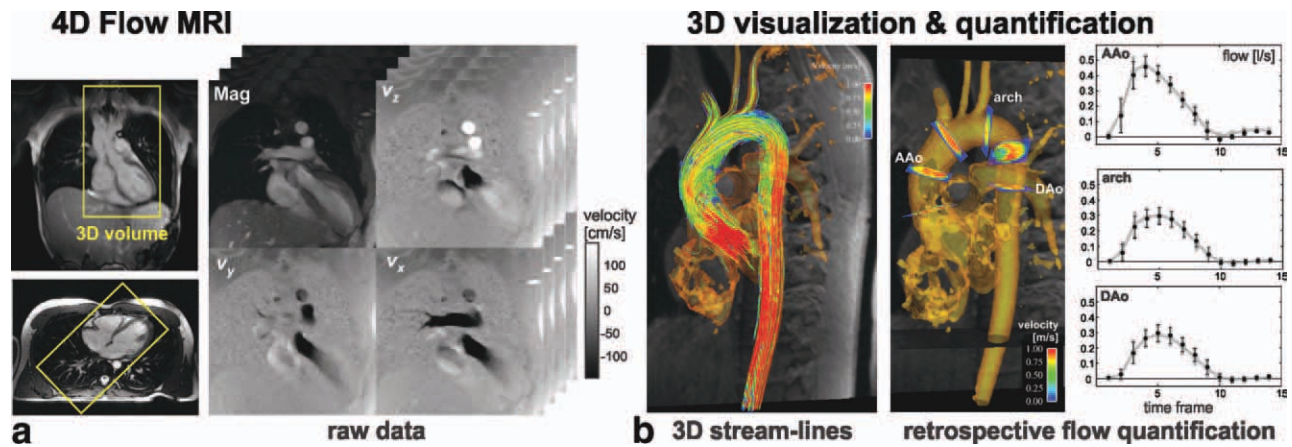


**Figure 7.** Acquisition of 4D Flow MRI data (a) and visualization and quantification of 3D hemodynamics (b) in the aorta. The 4D Flow raw data comprises information along all three spatial dimension, three velocity directions, and time in the cardiac cycle. A 3D PC-MRA (B, iso-surface rendering of the aorta) can be calculated from the 4D flow data to aid visualization (here: systolic 3D streamlines) and placement of analysis planes for retrospective flow quantification. [Color figure can be viewed in the online issue, which is available at [wileyonlinelibrary.com](http://wileyonlinelibrary.com).]

phase contrast techniques, characterization of complex flow patterns became easier to perform and more compelling to visualize (11,12,81). Software has been developed to extend analysis beyond simple visualization of aortic flow by allowing estimation of key secondary vascular parameters that can be correlated with aberrant flow patterns (20,27,31,32). The goal of current research is to understand how this abnormal flow may promote or worsen vascular disease so that 4D flow imaging can be used in the clinical evaluation and management of patients with aortic disease.

Recent work has focused on gross pathologies of the thoracic aorta such as coarctation and aneurysm. MRI flow evaluation has long been a component of the clinical management of patients with aortic coarctation, and recent studies suggest that 4D flow imaging may expand this role. Not only can collateral flow be reliably calculated and aortic flow profiles readily assessed, but also abnormal 3D flow patterns can be identified that correlate with postrepair complications including aneurysm and rupture (89–92). Aneurysms of the thoracic aorta are associated with complex abnormal flow patterns, many of which are helical in nature

(10,18,80,93,94). The significance of these patterns has been debated. Are they simply the consequence of a dilated aorta, or do they play an active role in the progression of aneurysms? In a subset of cases with aortic valve disease, recent work suggests that flow may play an active role. Similar flow to that seen within ascending aortic aneurysms has been demonstrated in aortas that are not (yet) dilated (95–97).

Evaluation of valve-related disease of the ascending aorta is a promising clinical application for 4D flow MRI. Many studies have assessed flow alterations in patients who have undergone aortic valve and/or ascending aortic replacement (17,98,99). But clinically, 4D flow MRI may prove useful in the presurgical stage by risk-stratifying patients and guiding the timing of intervention. Aortic valve disease is relatively common, especially in the elderly, and is associated with the long-observed phenomenon of poststenotic dilation of the ascending aorta (100,101). The mechanism has been presumed to be flow-related, but without 4D flow MRI the altered hemodynamics in the aortic root with aortic stenosis have not been well characterized. The uniquely detailed assessment that 4D flow MRI affords

Table 1  
4D Flow Sequence Parameters for Different Anatomic Regions

Region	Spatial resolution [mm]	Temporal resolution [ms]	Venc [cm/s]	Scan time [min]
Head				
Intracranial arteries	0.8–1.0	40–60	80	15–20
Neck				
Carotid arteries	1.0–1.2	40–50	100–200	10–15
Thorax				
Aorta	2.0–2.5	40–50	150–200	10–20
Pulmonary artery	2.0–2.5	40–50	100–150	10–20
Whole heart	2.5–3.0	40–50	150–200	15–25
Abdomen				
Hepatic vessel (venous)	2.0–2.5	40–60	30–40	15–20
Hepatic vessel (arterial)	1.5–2.0	40–50	60–80	10–20
Renal arteries	1.0	40–80	40–80	8–12
Lower extremities				
Iliac & femoral arteries	1.0–1.5	40–80	80–120	10–20

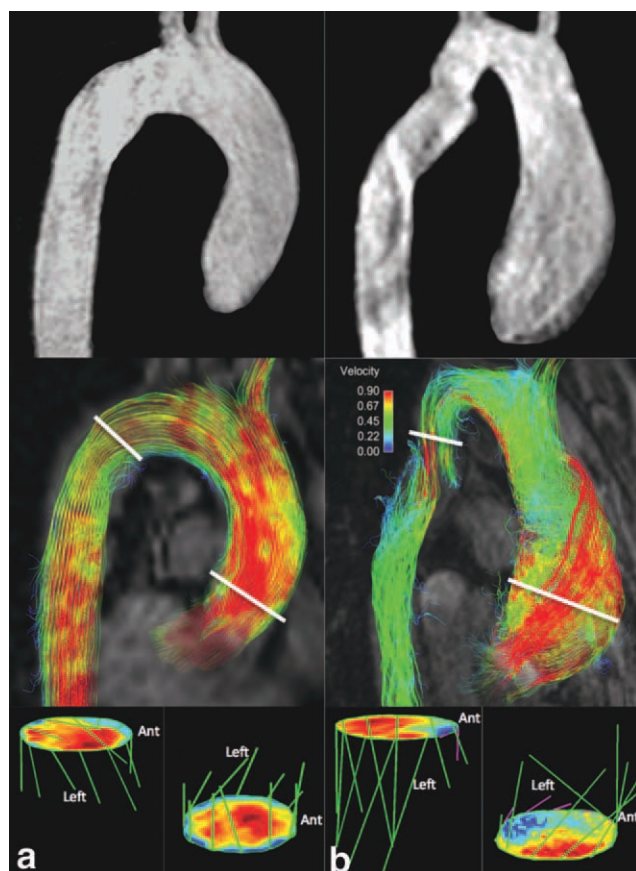


**Figure 8.** Abnormal systolic blood flow is demonstrated in a patient with stenotic bicuspid aortic valve, aortic root aneurysm, and mild coarctation. **a:** Normal blood flow for comparison in a healthy volunteer. From top to bottom, MRA, streamlines at peak systole, and cross-sectional wall shear stress analysis at the aortic root and proximal descending aorta are exhibited. The MRA reveals normal “candy-cane” geometry of the thoracic aorta and systolic streamlines that smoothly extend through the thoracic aorta. Cross-sectional analysis shows centralized flow in both the ascending and descending aorta and symmetrical wall shear stress around the vessel lumen (the relative magnitude is represented by the green bars). **b:** Identical analysis for a 24-year-old male with a stenotic bicuspid aortic valve, a progressively enlarging poststenotic aneurysm, and an unrepaired but mild coarctation. Systolic flow in the aortic root is notably eccentric, with high-velocity streamlines following a right-handed helix through the ascending aorta. The proximal cross-sectional analysis shows flow displaced along the right-anterior vessel wall, where shear stress is asymmetrically elevated. While deemed clinically insignificant, analysis in the region of the mild coarctation shows that slightly eccentric flow results in skewing of the shear stress profile. [Color figure can be viewed in the online issue, which is available at [wileyonlinelibrary.com](http://wileyonlinelibrary.com).]

of altered systolic flow has revealed eccentric flow jets with stenotic and deformed aortic valves (95,102). The degree of flow eccentricity can be quantified, and has been shown to correlate with focally elevated wall shear stress and aortic dilation (97,103–105). 4D flow MRI could thus potentially be a useful tool for risk stratification of the sizable population of patients with aortic valve disease for aneurysm development.

To highlight key differences between normal and abnormal flow features associated with pathology, a simplified assessment of flow in the thoracic aorta is presented using streamlines at peak systole and cross-sectional analysis of wall shear stress (Fig. 8). Normal flow is fastest centrally, gives rise to streamlines that smoothly wrap through the thoracic aorta, and results in a relatively even distribution of wall shear stress around the aortic circumference at the planes depicted (Fig. 8a). In contrast to these normal flow features, aberrant and complex peak systolic flow is presented for a patient with a bicuspid aortic valve, an ascending aortic aneurysm and mild aortic coarctation (Fig. 8b). Eccentric systolic flow gives rise to helical streamlines through the ascending aorta and a skewed shear stress profile with focal elevation in the right-anterior quadrant of the ascending aorta. Flow abnormalities are also seen at the site of a mild aortic coarctation. A region of mild narrowing causes displacement of flow from the vessel center, resulting in a skewed shear stress profile.

#### *Detection of a New Potential Pathomechanism: Aortic Plaques and Stroke*

Plaques of the ascending aorta and aortic arch have been known as a relevant cause of embolic stroke for over 20 years (106,107). Although the incidence of complex aortic plaques is highest in the proximal descending aorta, such plaques are only considered an embolic source of stroke in the unlikely coincidence of severe aortic valve insufficiency causing retrograde flow and embolization in case of plaque rupture. Because the descending aorta is distal to the left subclavian artery and retrograde embolization was thought to be unlikely, these plaques have not usually been considered a potential source of stroke (108,109).

There is growing evidence, however, that diastolic retrograde flow in the descending aorta may be a frequent phenomenon in the presence of atherosclerosis, as shown in Fig. 9. Importantly, diastolic retrograde flow in the descending aorta may represent an overlooked mechanism of retrograde embolization in stroke patients. The underlying physiology is related to the increased aortic stiffness due to aortic atherosclerosis. Consequently, increased pulse wave velocity and earlier wave reflection at the periphery can then result in marked diastolic retrograde descending aortic flow, even in the absence of aortic valve insufficiency (94,110,111).

4D flow MRI allows for the detailed visualization of aortic volumetric blood flow. In combination with an MRI protocol for 3D aortic plaque detection, retrograde embolization from complex descending aortic plaques was recently described as a proof-of-principle. In two separate studies ( $n = 63$  and  $n = 94$  stroke patients) the potentially underestimated role of descending aorta plaques was evaluated (112,113). Both studies showed that retrograde embolization was frequent and could reach all supraaortic arteries as a new pathomechanism for embolic stroke in all vascular territories. Moreover, this mechanism constituted the only probable source of retinal or cerebral

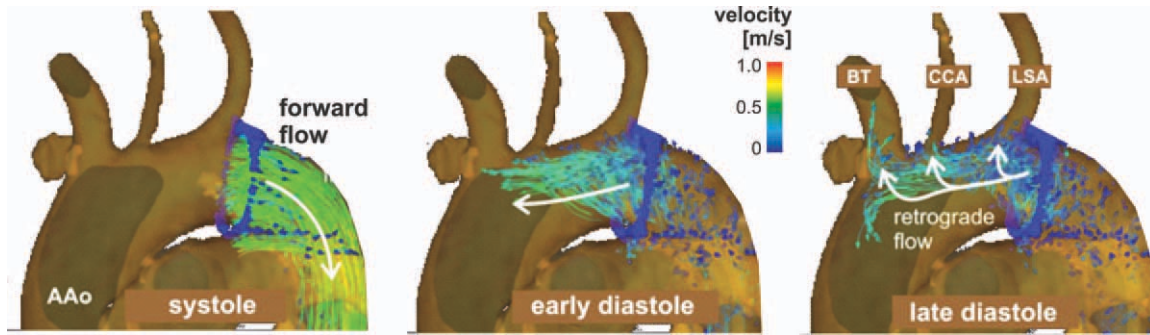


**Figure 9.** In vivo measurement and visualization of 3D blood flow in the proximal descending aorta using 4D flow MRI. Increased aortic stiffness in a patient with aortic atherosclerosis results in substantial diastolic retrograde flow as demonstrated by time-resolved 3D pathlines originating from an emitter plane in the proximal descending aorta (DAo). Diastolic retrograde flow clearly reaches all three brain feeding arteries and may provide a previously overlooked mechanism of retrograde embolization in stroke patients with high-risk plaques in the descending aorta. BT, brachiocephalic trunk; CCA, left common carotid artery; LSA, left subclavian artery; AAO, ascending aorta; DAo, descending aorta. [Color figure can be viewed in the online issue, which is available at [wileyonlinelibrary.com](http://wileyonlinelibrary.com).]

infarction in subgroups of patients with cryptogenic stroke etiology. Aortic valve insufficiency did not correlate with retrograde flow. These findings strongly indicate that complex descending aortic plaques should be considered a new embolic source of stroke even in the absence of aortic valve insufficiency.

#### *Pulmonary Arteries*

In pulmonary artery imaging 4D flow MRI has provided useful information in the evaluation of differential blood flows to the right and left pulmonary artery, eg, in postsurgical congenital heart disease (114). Moreover, in pulmonary hypertension (PAH), the routine interpretation of morphological determinants of PAH such as vessel diameters can be complemented by dynamic information and the visual and quantitative estimation of pressure gradients. A variety of indirect and, more important, noninvasive predictors for pulmonary artery pressure can be derived from 4D flow MR acquisitions. Sanz et al (115) have shown that average velocities and minimum pulmonary artery areas were the parameters with best diagnostic performance. Attempts to directly estimate PAH applying 2D PC MRI has shown high correlation with ultrasound and catheterization in the presence of tricuspid regurgitation. To estimate the pulmonary arterial pressure, the modified Bernoulli equation was used to determine the pressure gradient over the tricuspid valve, which was then multiplied with the mean right arterial pressure derived from the caval index (change in inferior vena cava size during inspiration) (116,117). Lastly, pressure differences can be directly derived from time-resolved phase contrast volumes with three-directional velocity encoding by solving the Navier–Stokes equation (118). However, this application has, so far, been restricted to the evaluation of systemic arterial vessels (55,119). The application to the pulmonary arteries is still warranted.

Besides quantitative approaches to 4D flow MRI data in PAH, the visualization of the acquired velocity fields with color-coded streamlines, time-resolved particle traces, and vector graphs can contribute to the

understanding of the severity of PAH. In a recent study, Reiter et al (120) presented visualization results using a multislab 4D flow MRI approach. In their comparison, gross blood flow trace patterns and their temporal behavior correlated well with invasive pressure readings. The detection of vortex flow in the main pulmonary artery (as shown in comparison to a normal volunteer in Fig. 10) is in line with recent findings from Helderma et al (121), who determined early retrograde flow in the proximal pulmonary vessels as a surrogate marker of PAH severity.

#### *4D Flow MRI in the Heart and Valves*

There are several studies that have investigated healthy and abnormal intraatrial and intraventricular blood flow based on 4D flow MRI (122). As a consequence of looping during embryonic development, the blood undergoes marked changes of direction through atrial, ventricular, and arterial compartments of the heart. Early work by Kilner et al (16) illustrated the asymmetries and direction-changes of flow in selected planes of acquisition through the chambers of the heart. The patterns of atrial and ventricular filling were reported to be asymmetric in ways that allow the momentum of inflowing blood to be redirected appropriately toward the next cavity. The changes of direction at the ventricular level are such that inertial recoil away from the ejected blood is in a direction that can enhance rather than inhibit ventriculo-atrial coupling, especially on exertion.

In the normal heart, flow patterns within the ventricles demonstrated asymmetric, regionally constrained ring vortices near mitral and tricuspid valves during diastolic inflow (16,123). 3D flow visualization based on time-resolved 3D pathlines revealed that blood entering the left ventricle (LV) during diastole that leaves the LV during systole within one heartbeat (direct flow) constitutes about one-third of the left ventricular end-diastolic volume (124,125). Patient studies have shown that the incidence, location, and extent of vortex flow inside the LV were markedly altered in patients with dilated cardiomyopathy. In

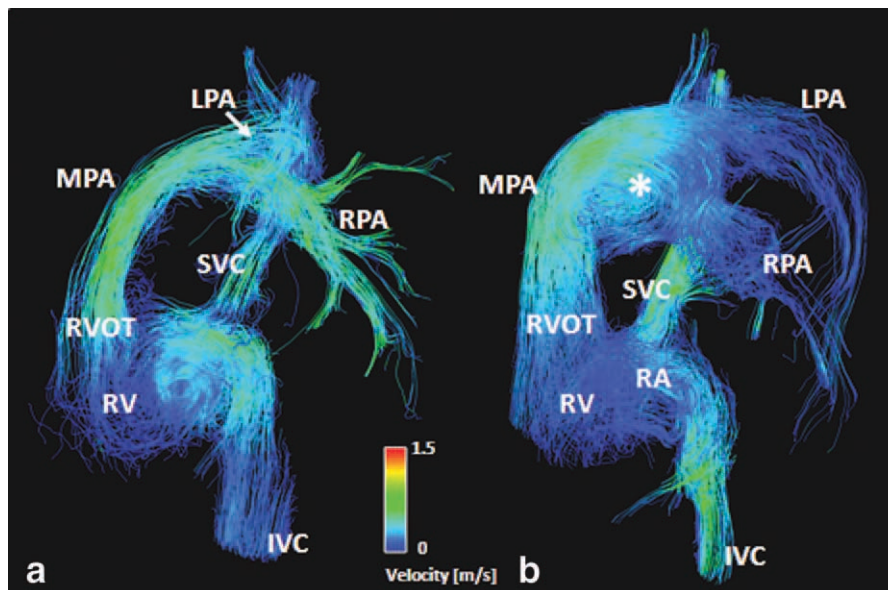


**Figure 10.** Color-coded streamline visualization of a PC VIPR scan in a healthy volunteer (a) and a 30-year-old man with pulmonary artery hypertension (b). The catheter-based mean pulmonary artery pressure (mPAP) in the patient was 60 mmHg, the right ventricular ejection fraction (EF) derived from cine bSSFP imaging was 43%. The differences in morphology and the development of a large vortical flow pattern in the main pulmonary artery (MPA, asterisk) can be clearly appreciated. Color-coding reflects absolute measured velocities. LPA, RPA, left and right main pulmonary artery; RVOT, right ventricular outflow tract; SVC, IVC, superior and inferior vena cava; RV, right ventricle; RA, right atrium. [Color figure can be viewed in the online issue, which is available at [wileyonlinelibrary.com](http://wileyonlinelibrary.com).]

addition, direct flow within the LV from the left atrium through the aortic valve was decreased in patients compared with healthy volunteers (125,126).

A number of previous reports demonstrated that 4D flow MRI with retrospective valve-tracking could accurately quantify net flow volumes and regurgitation through all four heart valves in patients with valvular insufficiency (17,21,127). In patients with valve stenosis and systolic high velocity jet flow, elevated turbulent intensity values have been reported in the heart for mild aortic and severe mitral regurgitation (32). Other studies have contributed to the understanding of postsurgical alterations such as the analysis of valvular hemodynamics after different valve-sparing aortic root replacements and the postsurgical vortex flow patterns in the sinuses of Valsalva (98,99). While the importance of maintaining sinuses in valve-sparing surgical repair of aortic root ectasia is still debated, an improved understanding of the hemodynamic consequences of these surgical interventions may provide a better understanding of the relationship between postsurgical aortic root geometry, flow characteristics, and valve function. A more detailed broad overview over the role of 4D flow in the ventricles, atria, and valves is provided in a recent review article (122).

#### Whole Heart 4D Flow

The feasibility of extending 4D flow MRI to the coverage of the whole heart and surrounding great vessels (left and right ventricles and atria, caval venous supply, the pulmonary arteries, and the thoracic aorta) has recently been demonstrated (70,128). However, currently available techniques still require long scan times on the order of 20 minutes or more for reasona-

ble spatial ( $\approx 2\text{--}3$  mm) and temporal (40–50 msec) resolution. Nevertheless, results from pilot studies indicate the potential of whole heart 4D flow MRI for the comprehensive analysis of postsurgical hemodynamics in the complex situation of congenital heart disease (57,114,129).

#### Hepatic and Portal Venous Flow

Liver cirrhosis is a common and serious disease that leads to changes in hepatic blood flow. However, there are only a limited number of reports on the examination of hepatic (130) and splanchnic arterial flow or flow in the portal venous system (130–137). This may be partly explained by the complexity of the hepatic and portal venous flow—there are three vascular beds of interest supporting the liver (hepatic arterial and portal venous inflow, hepatic venous drainage), all with markedly different velocity profiles. Together with the splanchnic circulation and the formation of portosystemic shunts in portal hypertension (PH), a large range of velocities needs to be covered and multiple imaging planes over a large volume are needed for comprehensive coverage. If a functional response, eg, to a meal challenge or provocation with drugs is to be investigated, all 2D exams have to be repeated.

Here, comprehensive 4D flow data acquisition strategies such as initially presented by Stankovic et al (138) offer several advantages. In their study, the visualization of volumetric velocity maps was successful in characterizing various flow field patterns. In the initial comparison to ultrasound in five cirrhotic patients, moderate correlations of peak and mean velocities were determined, where the differences were probably due to temporal averaging during the 4D

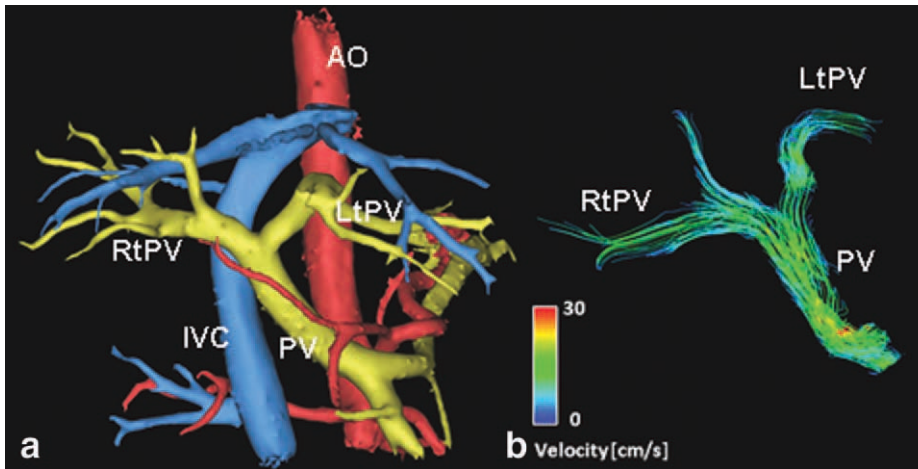


**Figure 11.** Vascular segmentation (a) and portal venous flow patterns visualized with color-coded streamlines (b) in a 67-year-old man with liver cirrhosis. In a, the abdominal vasculature is visualized on the basis of a PC angiogram (yellow = portal venous, blue = systemic venous, red = arterial vasculature). PV, portal vein; LTPV, RtPV, left and right portal venous branch; IVC, inferior vena cava; AO, abdominal aorta. [Color figure can be viewed in the online issue, which is available at [wileyonlinelibrary.com](http://wileyonlinelibrary.com).]

acquisition. More recent results in 20 patients and 40 young and age-matched controls showed a significant correlation of 4D MRI with the reference standard Doppler ultrasound for maximum and mean velocities and flow for the intrahepatic vessels. Quantitative flow analysis revealed significant alterations in velocities and flow in cirrhosis patients compared with age-matched and younger control groups (139).

By extending the acquisition field of view to the entire abdomen with the radially undersampled acquisition scheme PC VIPR (46), the entire portal venous system, systemic venous, and arterial flow patterns have been analyzed (see Fig. 11). Initial results in patients with cirrhosis have been presented (59). The wide range of velocities of interest in this vascular territory is challenging. In these studies, a 5-point velocity-encoding scheme introduced by Johnson and Markl (40) was used in order to increase the range of the aliasing-free velocity sensitivity while preserving the VNR of a lower  $V_{enc}$  acquisition at the expense of a fairly short scan time extension of 20%. Alternatively, dual- $V_{enc}$  encoding might be better suited to address low portal venous velocities while simultaneously being able to accurately measure arterial flows (140,141). The comprehensive vascular coverage provides an interesting approach for future studies of the hemodynamics in portal hypertension, including changes during the course of the day (diurnal changes) and after ingestion of meal.

### Renal Arteries

Renal artery stenosis is a recognized cause of hypertension and progressive renal insufficiency and occurs in up to 45% of patients with peripheral vascular disease (142). Proper assessment of the hemodynamic significance of renal artery lesions is clinically important for treatment planning and monitoring for patients with vascular disease as well as for kidney transplant donors and recipients. A lesion that narrows the luminal diameter by 75% or more is usually of hemodynamic significance. In cases of a mild stenosis (less than 50%), no intervention is typically required. However, the hemodynamic significance of a stenosis measured as 50%–75% cannot be reliably derived from vessel diameter measurements alone. In

such cases, intraarterial pressure measurements are obtained under x-ray angiography (143).

MRI of the renal vasculature is challenging because of the relatively small vessel diameter, especially of segmental branches, a sometimes torturous vessel path, and complex motion of the renal vessels throughout the cardiac and the respiratory cycle. Contrast-enhanced (CE) MRA is commonly used for renal artery stenosis assessment. However, patients with compromised kidney function, including kidney transplant donors and recipients, should not receive gadolinium-based contrast agents because of the risk for nephrogenic systemic fibrosis (144).

PC MRI has been used to assist in the diagnosis of renal artery stenosis in several ways. Schoenberg et al (145) showed that the presence of hemodynamically significant stenosis is identified by a delayed and widened peak in the flow waveforms of 2D cine PC measurements performed perpendicular to each renal artery at a proximal location. Prince et al (146) proposed the use of a nongated 3D PC sequence. They demonstrated correlation of signal voids distal to a lesion with presence of stenosis >70% due to intra-voxel dephasing in this region of turbulent flow.

More recently, 4D flow MRI with a radially undersampled trajectory has been applied to this vascular territory (Fig. 12). Free-breathing acquisitions of  $\approx 10$  minutes provide angiograms of abdominal arteries and veins with good correlation of diameter measures across various vessel sizes (52) as an alternative to contrast enhanced MRA. PC VIPR demonstrated superior visualization of segmental renal arteries because of decreased kidney-vessel contrast in CE MRA from parenchymal enhancement. In addition, the functional information can be used for the noninvasive assessment of hemodynamic significance of renal artery stenosis, as shown in Fig. 12e,f. As validated in an animal study, transstenotic pressure gradients derived from the velocity fields correlated well with measurements obtained invasively with pressure wires (56).

### Carotid Arteries

In the normal carotid bifurcation, the application of 4D flow MRI demonstrated complex 3D blood flow

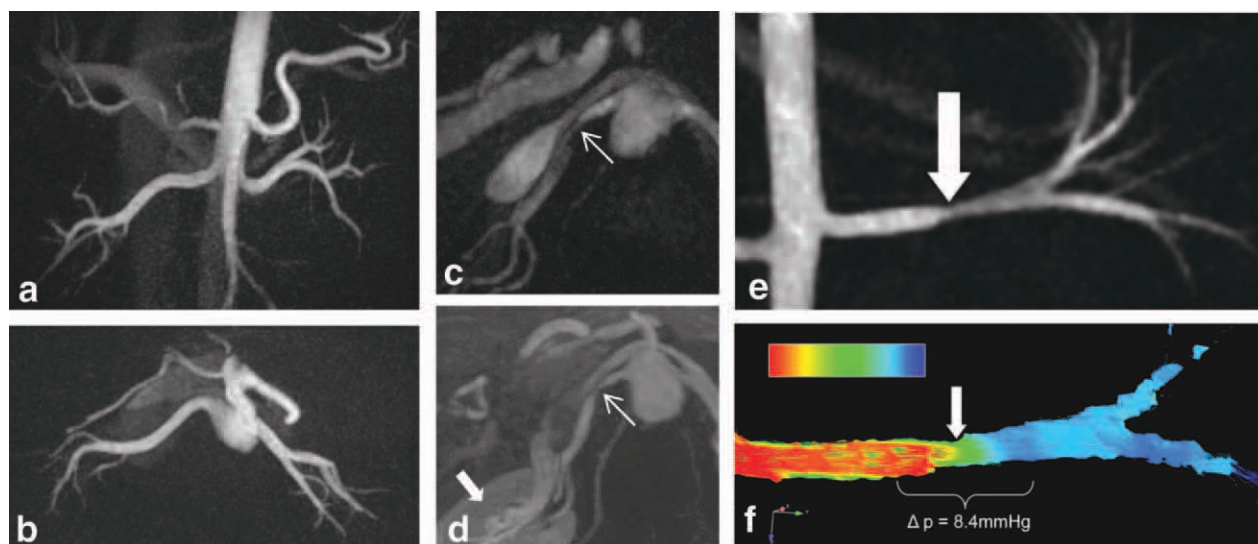


**Figure 12.** Renal artery imaging with 4D flow MRI. All flow images were acquired with a 10-minute free-breathing PC VIPR acquisition. **a,b:** Coronal and limited axial maximum intensity projection of a PC MRA of a healthy volunteer demonstrate high contrast, good reformatting capabilities, and coverage of the entire abdomen. **c,d:** reformatted maximum intensity projections of a patient with a right renal artery stenosis (thin arrow) show good agreement of the PC VIPR acquisition (c) and the CE MRA (d). Also note the enhancement of the renal parenchyma from the contrast uptake in (d). **e,f:** PC MRA (e) and corresponding pressure difference map (f) as derived from the velocity fields via Navier–Stokes equations in a swine model with renal artery stenosis (wide arrow). [Color figure can be viewed in the online issue, which is available at [wileyonlinelibrary.com](http://wileyonlinelibrary.com).]

patterns such as helical flow in the proximal and naturally bulbic internal carotid artery (ICA), as shown in Fig. 13 (147). In patients with ICA stenosis, markedly altered filling and helix formation in the ICA bulb was observed while revascularization partly restored normal filling and helix formation (84). Furthermore, a direct comparison of mean and absolute flow velocities in the common carotid artery (CCA) between 4D flow MRI and Doppler ultrasound showed good agreement despite general underestimation of peak velocities by MRI.

Since carotid artery stenosis is a leading cause of ischemic stroke, detailed insights into the causes for the development of atherosclerosis at this site are of interest. Among other risk factors, it is assumed that the development of atherosclerosis in the naturally bulbic ICA is related to local hemodynamic conditions such as flow deceleration or recirculation associated with reduced and oscillating wall shear stress (WSS) (148). Particularly, low absolute WSS and high oscillatory shear index (OSI) are hypothesized to determine the composition of atherosclerotic lesions and the development of high-risk plaques (149,150). Since blood flow through the carotid bifurcation is complex, with nonsymmetric flow profiles, the full three-directional velocity information as provided by 4D flow MRI is needed for a complete *in vivo* assessment of the segmental distribution of WSS (20).

A recent study analyzing WSS in the normal carotid bifurcation confirmed that potentially atherogenic wall parameters were predominantly concentrated at the posterior wall of the proximal ICA (84). This is in concordance with the tendency of carotid atherosclerosis to affect the outer walls of arterial bifurcations and to mostly develop in the proximal part of the ICA

bulb, as shown in Fig. 13. Moreover, a significant relationship between the size of regions exposed to altered wall parameters and the individual bifurcation geometry was demonstrated, similar to a recent study using carotid bifurcation geometry and computational fluid dynamics (CFD) (148). In contrast, patients with moderate ICA stenosis revealed a clearly altered distribution of wall parameters. Low WSS and high OSI moved downstream to the ICA plaque potentially linked to future growth of such lesions. In patients after surgical recanalization of former high-grade ICA stenosis, the wall parameter distribution was similar to that observed in healthy volunteers. 4D flow MRI could thus be a valuable technique to assess the individual risk of flow-mediated atherosclerosis and carotid plaque progression.

### **Intracranial Hemodynamics**

To date, intracranial 4D flow MRI has predominantly been applied to determine feasibility in normal subjects and depict flow patterns in patients with intracranial aneurysms (151–153). Bammer et al (151) have successfully visualized the temporal and spatial evolution of helical patterns of blood flow in the carotid siphon. Also, they studied the effects of magnetic field strength, parallel imaging, and temporal resolution on intracranial 4D flow MR data. Their results indicated that studies were consistently performed faster at 3T than at 1.5T because of better parallel imaging performance. A high temporal resolution (65 msec) was required to follow dynamic processes in the intracranial vessels. In general, 4D flow MRI provided a high degree of vascular conspicuity.

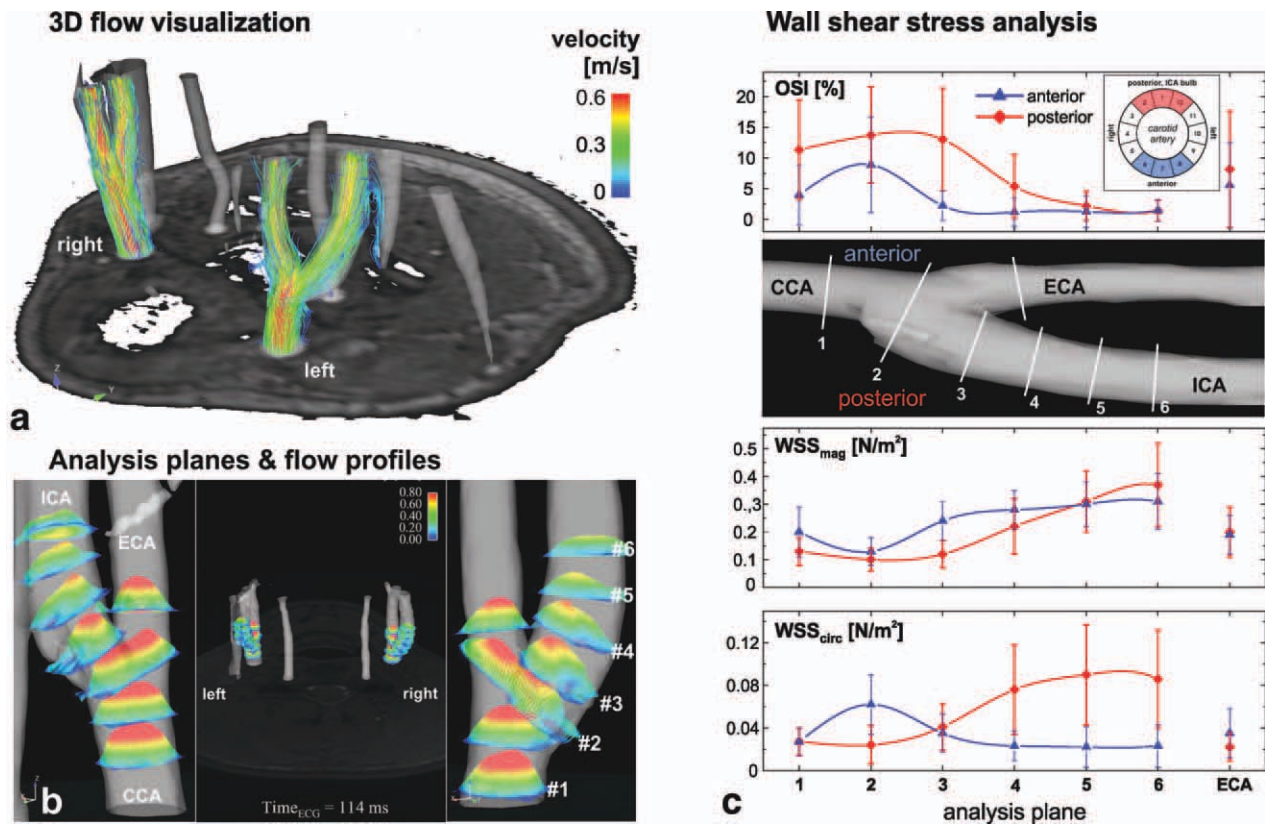


**Figure 13.** Carotid 4D flow MRI and wall shear stress analysis. **a:** 3D PC-MRA and 3D flow visualization in a normal carotid bifurcation. Streamline visualization shows 3D blood flow in the left and right carotid bifurcations. **b:** Retrospectively positioned analysis planes can be used to illustrate regional flow profiles in the left and right carotid bifurcation. Consistent placement of equidistant planes (#1–6) permits quantification of wall shear stress along the lumen circumference (eg, for 12 segments as shown here). **c:** Results of a study with 64 normal carotid arteries shows the distribution of absolute wall shear stress ( $WSS_{mag}$ ), oscillatory shear index (OSI), and the circumferential WSS component ( $WSS_{circ}$ ). WSS (OSI) in the posterior ICE bulb (red curves) was clearly reduced (increased) compared with anterior regions (blue curves). Different and potentially atherogenic low WSS and high OSI in the ICA bulb compared with other segments may help explaining why ICA stenoses predominantly develop and progress at this location. ICA, internal carotid artery; ECA, external carotid artery; CCA, common carotid artery. [Color figure can be viewed in the online issue, which is available at [wileyonlinelibrary.com](http://wileyonlinelibrary.com).]

In studies with intracranial aneurysms, complex and vortical flow patterns were commonly seen inside the aneurysm, as shown for a patient with a giant aneurysm in Fig. 14 (154–158). The magnitude as well as both the spatial and temporal evolution of vortical flow patterns differed markedly among different investigated aneurysms. Temporally varying flow patterns were observed in wide-necked aneurysms (high aspect ratio) while temporally more stable vortex flow was seen in aneurysms with lower aspect ratio. The subsequent estimation of wall parameters such as segmental WSS inside cerebral aneurysms revealed reduced values relative to the parent artery in the majority of the investigated cases. These results support the hypothesis that regions with low WSS may promote aneurysm growth, which was recently confirmed by a study based on computational fluid dynamics (CFD) (159). A direct comparison of aneurysmal hemodynamics between 4D flow MRI and CFD in a small number of patients by Bousset et al (157) revealed good agreement for flow patterns and velocities. However, large discrepancies for wall parameters such as the WSS indicated the need for larger cohorts for com-

parisons and potentially improved spatial resolution and analysis strategies.

### Peripheral Vessels and Peripheral Arterial Occlusive Disease

Peripheral arterial occlusive disease (PAOD) is commonly explored with basic clinical tests such as the ankle-brachial-index (ABI), constant load treadmill test, and Doppler ultrasound due to its excellent temporal and spatial resolution. However, computed tomography angiography (CTA) and even more so CE MRA are nowadays routinely used for PAOD assessment. Although phase contrast imaging was originally used to obtain MRA images (160–163), some authors have used the quantitative information inherent in MR phase contrast scans to derive information on the severity of PAOD. Similar to Doppler ultrasound, the waveforms derived in locations superior or inferior to stenoses or simply in two locations on the proximal and distal leg can be used to characterize the severity of PAOD (164,165). Changes from normal triphasic waveforms upstream of a stenosis to monophasic

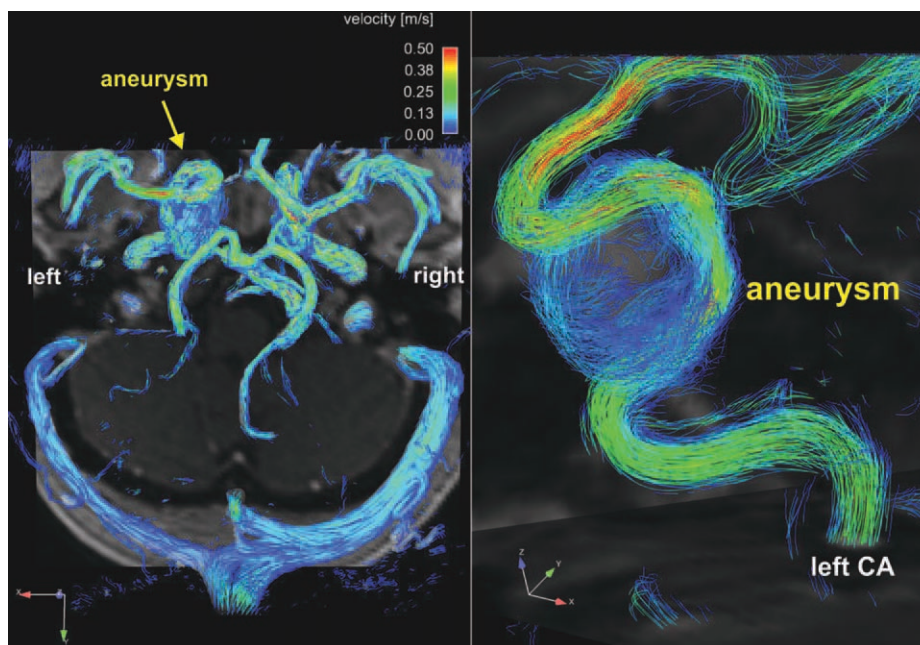


**Figure 14.** Time-integrated pathlines illustrating flow patterns in the large intracranial arteries and a giant cranial aneurysm in the left hemisphere. A marked vortical flow pattern with flow channels mostly confined to regions near the aneurysm wall can clearly be appreciated. CA, carotid artery. [Color figure can be viewed in the online issue, which is available at [wileyonlinelibrary.com](http://wileyonlinelibrary.com).]

waveforms downstream of a stenosis are typical for high-grade stenosis (166,167).

In a similar fashion to other applications described in this review, 4D flow MRI has been qualitatively and quantitatively applied to the peripheral arteries (168). Next to the simultaneous coregistration of morphology and hemodynamic information, the intrinsically high signal of 3D acquisitions can be exploited in order to gather sufficient signal in these comparably small vessels. This advantage, however, has to be weighed against the limited resolution obtained with available 4D flow MRI approaches due to scan time limitations.

Future research is warranted to extend previously published feasibility results to longitudinal and comparative studies investigating the potential impact of 4D flow MRI in PAOD. To address existing shortcomings, an optimized spatial resolution probably at isotropic 1 mm is advisable.

## DISCUSSION

4D flow MRI is an evolving technology based on the basic principle of PC MRI. It has recently gained increased importance due to new developments in MR methodology and data analysis capabilities. Its potential to provide a comprehensive evaluation of vascular hemodynamics with full volumetric coverage is promising for future cardiac and vascular diagnostics (169). Although pulse sequences for 4D flow MRI continue to be developed, its accuracy and test-retest reliability have been and are constantly demonstrated in various phantom and *in vivo* studies (23,83). Applications of 4D flow MRI in patient studies in different anatomic regions from “head to toe” have underlined its feasibility in a clinical environment.

Information of blood flow can also be obtained by standard 2D CINE PC techniques that can easily be applied during a single breath hold, which may be sufficient for several clinical applications. 4D flow MRI, on the other hand, offers the ability of retrospective quantitative evaluation of blood flow at any location of interest within the 3D volume. Despite relative long scan times, on the order of 5–20 minutes (depending on heart rate, breathing compensation efficiency, and applied sequence), 4D flow MRI inherently provides an easy scan prescription (positioning of a single 3D volume). This may be especially advantageous in cases where multiple breath-held 2D CINE PC MRI scans are needed such as in congenital heart disease. Particularly in young pediatric patients, where breath-held scans are often not feasible, the free-breathing 4D flow MRI acquisition with volumetric converge may provide an advantage over standard MR techniques. Whole heart 4D flow MRI may open a new chapter in diagnosing congenital heart disease, potentially preventing these patients from ionizing radiation exposure and/or catheterizations as their disease state can be regularly monitored throughout their life.

Current limitations of 4D flow MRI include long scan times and limited spatial resolution for flow analysis in smaller vessels. New development based on multidimensional parallel imaging (such as *k-t* parallel imaging) or sparse sampling techniques (radial acquisitions, compressed sensing, and others) are particularly promising for 4D flow MRI (42,43,48,170,171). Data undersampling along multiple dimension (space, time, velocity encoding) has the potential to substantially accelerate 4D flow MR image acquisition and/or significantly improve spatiotemporal resolution. Early results indicate that acceleration

factors on the order of 4–6 can be achieved. This could reduce the total acquisition time of Cartesian aortic 4D flow MRI from currently 15–20 to 5–8 minutes. Moreover, the combination with high albumin binding (so-called “bloodpool”) contrast agents may help to offset SNR loss associated with high acceleration factors and increased spatial resolution for imaging of small vessels (172).

The interest in “dual  $V_{enc}$ ” acquisitions, ie, simultaneous encoding with two different  $V_{enc}$ s, is currently under exploration. Especially in situations with neighboring slow and fast flows (such as in the heart or the liver), techniques with an increased spectrum of velocity-encoding sensitivities could provide tremendous improvements to the diagnostic value of 4D flow MRI. The intelligent combination of high  $V_{enc}$  (to avoid aliasing in fast flows) and low  $V_{enc}$  (to obtain high SNR contrast in slow flow conditions) acquisitions has not been sufficiently addressed so far and warrants further research efforts.

It should be noted that the 4D flow MRI techniques discussed in this article and are often not commonly available on clinical routine MR systems. The applications presented in this review article and research groups active in this area of research often rely on MR sequences that are not commercially available. Increased efforts by the MR research community and the MR vendors are needed to afford a more widespread availability of optimized 4D flow MRI techniques.

A further limitation of current 4D flow MRI protocols is related to the lack of standardized preprocessing tools and software packages for visualization and retrospective quantification. Although there are various developments with the aim to streamline and standardize data analysis and visualization strategies, more clinical studies and test–retest analysis are needed to prove the validity of available software solutions. Similarly, there is limited knowledge regarding the repeatability of results between hardware and software vendors, which is vital to the techniques’ clinical acceptance. A secondary challenge associated with data analysis is related to the efficient integration of the resulting data (3D visualization, hemodynamic parameters) into the clinical workflow and transfer of initial findings into longitudinal clinical studies.

In addition to the limited standards discussed above that need to be taken into account when comparing 2D or 4D flow data from different scanners or software packages, comprehensive flow visualization bears specific limitations that must not be overlooked. Specifically, the underlying acquisition scheme with multiple acquisitions to encode for single timepoints as well as the measurement over relatively long time spans (on the order of 5–20 minutes) implies averaging over potential small cyclic variations in the blood flow patterns as well as of nonperiodic “events” during blood flow that may occur occasionally but not throughout the whole measurement. In its most basic form this leads to temporally averaging that potentially decreases the peak velocity or flow measurements. Similarly, visualization options such as time-resolved pathlines are based on information in successive time-frames and the inherent error in the

measurement can thus increase by accumulating uncertainties from frame to frame. Further, similar to gray-scale depiction of 2D phase contrast values or vectors, color-coding has not been standardized. Therefore, color scales in images on display are a prerequisite for meaningful interpretation of data.

Similar to 4D flow MRI, computational fluid dynamics (CFD) provide insights to 3D blood flow and wall shear stress distribution in realistic vascular geometries (148,157,159). CFD results can be obtained with much higher spatial and temporal resolution than MR measurements but it is subject of ongoing debates of how boundary conditions needed for the CFD calculations (rigid walls, idealized in-flow velocity profiles, non-Newtonian blood models) affect the results. Here, the opportunity to measure complex geometries and associated flow fields in vivo holds promise to be combined with CFD for cross-validation and mutual enhancement of the diagnostic information.

In summary, 4D flow MRI, an emerging tool for the comprehensive evaluation of cardiovascular hemodynamics with full volumetric coverage, is a continuously developing field of research. Current implementations permit its integration into clinical protocols on the premises that scan times need to be further reduced and subsequent data analysis is successfully integrated into the clinical workflow. Overall, the increasing amount of available studies and applications of 4D flow MRI to vascular territories throughout the human body underline its potential for an improved understanding of the link between altered hemodynamics and cardiovascular disease.

## REFERENCES

1. Carr HY, Purcell EM. Effects of diffusion on free precession in nuclear magnetic resonance experiments. *Phys Rev* 1954;94:30–38.
2. Hahn EL. Detection of sea water motion by nuclear precession. *J Geophys Res* 1960;65.
3. Moran PR. A flow velocity zeugmatographic interlace for NMR imaging in humans. *Magn Reson Imaging* 1982;1:197–203.
4. Bryant DJ, Payne JA, Firmin DN, Longmore DB. Measurement of flow with NMR imaging using a gradient pulse and phase difference technique. *J Comput Assist Tomogr* 1984;8:588–593.
5. Van Dijk P. Direct cardiac NMR imaging of heart wall and blood flow velocity. *J Comput Assist Tomogr* 1984;171:429–436.
6. Nayler GL, Firmin DN, Longmore DB. Blood flow imaging by cine magnetic resonance. *J Comput Assist Tomogr* 1986;10:715–722.
7. Pelc NJ, Herfkens RJ, Shimakawa A, Enzmann DR. Phase contrast cine magnetic resonance imaging. *Magn Reson Q* 1991;7:229–254.
8. Chai P, Mohiaddin R. How we perform cardiovascular magnetic resonance flow assessment using phase-contrast velocity mapping. *J Cardiovasc Magn Reson* 2005;7:705–716.
9. Firmin DN, Gatehouse PD, Konrad JP, Yang GZ, Kilner PJ, Longmore DB. Rapid 7-dimensional imaging of pulsatile flow. *Comput Cardiol IEEE Comput Soc Lond* 1993;14:353–356.
10. Bogren HG, Mohiaddin RH, Yang GZ, Kilner PJ, Firmin DN. Magnetic resonance velocity vector mapping of blood flow in thoracic aortic aneurysms and grafts. *J Thorac Cardiovasc Surg* 1995;110:704–714.
11. Wigstrom L, Sjoqvist L, Wranne B. Temporally resolved 3D phase-contrast imaging. *Magn Reson Med* 1996;36:800–803.
12. Markl M, Chan FP, Alley MT, et al. Time-resolved three-dimensional phase-contrast MRI. *J Magn Reson Imaging* 2003;17:499–506.
13. Bogren HG, Mohiaddin RH, Kilner PJ, Jimenez-Borreguero LJ, Yang GZ, Firmin DN. Blood flow patterns in the thoracic aorta studied with three-directional MR velocity mapping: the effects

- of age and coronary artery disease. *J Magn Reson Imaging* 1997;7:784–793.
14. Buonocore MH. Visualizing blood flow patterns using streamlines, arrows, and particle paths. *Magn Reson Med* 1998;40:210–226.
  15. Wigstrom L, Ebberts T, Fyrenius A, et al. Particle trace visualization of intracardiac flow using time-resolved 3D phase contrast MRI. *Magn Reson Med* 1999;41:793–799.
  16. Kilner PJ, Yang GZ, Wilkes AJ, Mohiaddin RH, Firmin DN, Yacoub MH. Asymmetric redirection of flow through the heart. *Nature* 2000;404:759–761.
  17. Kozerke S, Hasenkam JM, Pedersen EM, Boesiger P. Visualization of flow patterns distal to aortic valve prostheses in humans using a fast approach for cine 3D velocity mapping. *J Magn Reson Imaging* 2001;13:690–698.
  18. Frydrychowicz A, Harloff A, Jung B, et al. Time-resolved, 3-dimensional magnetic resonance flow analysis at 3 T: visualization of normal and pathological aortic vascular hemodynamics. *J Comput Assist Tomogr* 2007;31:9–15.
  19. Hope TA, Markl M, Wigstrom L, Alley MT, Miller DC, Herfkens RJ. Comparison of flow patterns in ascending aortic aneurysms and volunteers using four-dimensional magnetic resonance velocity mapping. *J Magn Reson Imaging* 2007;26:1471–1479.
  20. Stalder AF, Russe MF, Frydrychowicz A, Bock J, Hennig J, Markl M. Quantitative 2D and 3D phase contrast MRI: optimized analysis of blood flow and vessel wall parameters. *Magn Reson Med* 2008;60:1218–1231.
  21. Roes SD, Hammer S, van der Geest RJ, et al. Flow assessment through four heart valves simultaneously using 3-dimensional 3-directional velocity-encoded magnetic resonance imaging with retrospective valve tracking in healthy volunteers and patients with valvular regurgitation. *Invest Radiol* 2009;44:669–675.
  22. Valverde I, Simpson J, Schaeffter T, Beerbaum P. 4D phase-contrast flow cardiovascular magnetic resonance: comprehensive quantification and visualization of flow dynamics in atrial septal defect and partial anomalous pulmonary venous return. *Pediatr Cardiol* 2010;31:1244–1248.
  23. Markl M, Wallis W, Harloff A. Reproducibility of flow and wall shear stress analysis using flow-sensitive four-dimensional MRI. *J Magn Reson Imaging* 2011;33:988–994.
  24. Oyre S, Paaske WP, Ringgaard S, et al. Automatic accurate non-invasive quantitation of blood flow, cross-sectional vessel area, and wall shear stress by modelling of magnetic resonance velocity data. *Eur J Vasc Endovasc Surg* 1998;16:517–524.
  25. Oshinski JN, Ku DN, Mukundan S Jr, Loth F, Pettigrew RI. Determination of wall shear stress in the aorta with the use of MR phase velocity mapping. *J Magn Reson Imaging* 1995;5:640–647.
  26. Frydrychowicz A, Stalder AF, Russe MF, et al. Three-dimensional analysis of segmental wall shear stress in the aorta by flow-sensitive four-dimensional-MRI. *J Magn Reson Imaging* 2009;30:77–84.
  27. Markl M, Wallis W, Bredecke S, Simon J, Frydrychowicz A, Harloff A. Estimation of global aortic pulse wave velocity by flow-sensitive 4D MRI. *Magn Reson Med* 2010;63:1575–1582.
  28. Bolster BD Jr, Atalar E, Hardy CJ, McVeigh ER. Accuracy of arterial pulse-wave velocity measurement using MR. *J Magn Reson Imaging* 1998;8:878–888.
  29. Tyszka JM, Laidlaw DH, Asa JW, Silverman JM. Three-dimensional, time-resolved (4D) relative pressure mapping using magnetic resonance imaging. *J Magn Reson Imaging* 2000;12:321–329.
  30. Ebberts T, Wigstrom L, Bolger AF, Wranne B, Karlsson M. Noninvasive measurement of time-varying three-dimensional relative pressure fields within the human heart. *J Biomech Eng* 2002;124:288–293.
  31. Bock J, Frydrychowicz A, Lorenz R, et al. In vivo noninvasive 4D pressure difference mapping in the human aorta: phantom comparison and application in healthy volunteers and patients. *Magn Reson Med* 2011;66:1079–1088.
  32. Dyverfeldt P, Kvitting JP, Sigfridsson A, Engvall J, Bolger AF, Ebberts T. Assessment of fluctuating velocities in disturbed cardiovascular blood flow: in vivo feasibility of generalized phase-contrast MRI. *J Magn Reson Imaging* 2008;28:655–663.
  33. Dyverfeldt P, Gardhagen R, Sigfridsson A, Karlsson M, Ebberts T. On MRI turbulence quantification. *Magn Reson Imaging* 2009;27:913–922.
  34. Dumoulin CL, Souza SP, Walker MF, Wagle W. Three-dimensional phase contrast angiography. *Magn Reson Med* 1989;9:139–149.
  35. Bernstein MA, Shimakawa A, Pelc NJ. Minimizing TE in moment-nulled or flow-encoded two- and three-dimensional gradient-echo imaging. *J Magn Reson Imaging* 1992;2:583–588.
  36. Atkinson DJ, Edelman RR. Cineangiography of the heart in a single breath hold with a segmented turboFLASH sequence. *Radiology* 1991;178:357–360.
  37. Thomsen C, Cortsen M, Sondergaard L, Henriksen O, Stahlberg F. A segmented k-space velocity mapping protocol for quantification of renal artery blood flow during breath-holding. *J Magn Reson Imaging* 1995;5:393–401.
  38. Markl M, Harloff A, Bley TA, et al. Time-resolved 3D MR velocity mapping at 3T: improved navigator-gated assessment of vascular anatomy and blood flow. *J Magn Reson Imaging* 2007;25:824–831.
  39. Pelc NJ, Bernstein MA, Shimakawa A, Glover GH. Encoding strategies for three-direction phase-contrast MR imaging of flow. *J Magn Reson Imaging* 1991;1:405–413.
  40. Johnson KM, Markl M. Improved SNR in phase contrast velocimetry with five-point balanced flow encoding. *Magn Reson Med* 2010;63:349–355.
  41. Thunberg P, Karlsson M, Wigstrom L. Accuracy and reproducibility in phase contrast imaging using SENSE. *Magn Reson Med* 2003;50:1061–1068.
  42. Baltes C, Kozerke S, Hansen MS, Pruessmann KP, Tsao J, Boesiger P. Accelerating cine phase-contrast flow measurements using k-t BLAST and k-t SENSE. *Magn Reson Med* 2005;54:1430–1438.
  43. Jung B, Honal M, Ullmann P, Hennig J, Markl M. Highly k-t-space-accelerated phase-contrast MRI. *Magn Reson Med* 2008;60:1169–1177.
  44. Glover GH, Pauly JM. Projection reconstruction techniques for reduction of motion effects in MRI. *Magn Reson Med* 1992;28:275–289.
  45. Barger AV, Peters DC, Block WF, et al. Phase-contrast with interleaved undersampled projections. *Magn Reson Med* 2000;43:503–509.
  46. Gu T, Korosec FR, Block WF, et al. PC VIPR: a high-speed 3D phase-contrast method for flow quantification and high-resolution angiography. *AJNR Am J Neuroradiol* 2005;26:743–749.
  47. Liu J, Redmond MJ, Brodsky EK, et al. Generation and visualization of four-dimensional MR angiography data using an undersampled 3-D projection trajectory. *IEEE Trans Med Imaging* 2006;25:148–157.
  48. Johnson KM, Lum DP, Turksi PA, Block WF, Mistretta CA, Wieben O. Improved 3D phase contrast MRI with off-resonance corrected dual echo VIPR. *Magn Reson Med* 2008;60:1329–1336.
  49. Glover GH, Noll DC. Consistent projection reconstruction (CPR) techniques for MRI. *Magn Reson Med* 1993;29:345–351.
  50. Larson AC, White RD, Laub G, McVeigh ER, Li D, Simonetti OP. Self-gated cardiac cine MRI. *Magn Reson Med* 2004;51:93–102.
  51. Stehning C, Bornert P, Nehrke K, Eggert H, Stuber M. Free-breathing whole-heart coronary MRI with 3D radial SSFP and self-navigated image reconstruction. *Magn Reson Med* 2005;54:476–480.
  52. Francois CJ, Lum DP, Johnson KM, et al. Renal arteries: isotropic, high-spatial-resolution, unenhanced MR angiography with three-dimensional radial phase contrast. *Radiology* 2011;258:254–260.
  53. Moftakhar R, Aagaard-Kienitz B, Johnson K, et al. Noninvasive measurement of intra-aneurysmal pressure and flow pattern using phase contrast with vastly undersampled isotropic projection imaging. *AJNR Am J Neuroradiol* 2007;28:1710–1714.
  54. Turk AS, Johnson KM, Lum D, et al. Physiologic and anatomic assessment of a canine carotid artery stenosis model utilizing phase contrast with vastly undersampled isotropic projection imaging. *AJNR Am J Neuroradiol* 2007;28:111–115.
  55. Lum DP, Johnson KM, Paul RK, et al. Transstenotic pressure gradients: measurement in swine—retrospectively ECG-gated 3D phase-contrast MR angiography versus endovascular pressure-sensing guidewires. *Radiology* 2007;245:751–760.
  56. Bley TA, Johnson KM, Francois CJ, et al. Noninvasive assessment of transstenotic pressure gradients in porcine renal artery stenoses using vastly undersampled phase contrast MR. *Radiology* 2011;261:266–273.
  57. Frydrychowicz A, Landgraf B, Wieben O, Francois CJ. Images in Cardiovascular Medicine. Scimitar syndrome: added value by

- isotropic flow-sensitive four-dimensional magnetic resonance imaging with PC-VIPR (phase-contrast vastly undersampled isotropic projection reconstruction). *Circulation* 2010;121:e434-436.
58. Chang W, Landgraf B, Johnson KM, et al. Velocity measurements in the middle cerebral arteries of healthy volunteers using 3D radial phase-contrast HYPRFlow: comparison with transcranial Doppler sonography and 2D phase-contrast MR imaging. *AJNR Am J Neuroradiol* 2011;32:54-59.
  59. Frydrychowicz A, Landgraf BR, Niespodzany E, et al. Four-dimensional velocity mapping of the hepatic and splanchnic vasculature with radial sampling at 3 Tesla: a feasibility study in portal hypertension. *J Magn Reson Imaging* 2011;34:577-584.
  60. Ehman RL, Felmlee JP. Adaptive technique for high-definition MR imaging of moving structures. *Radiology* 1989;173:255-263.
  61. McConnell MV, Khasgiwala VC, Savord BJ, et al. Comparison of respiratory suppression methods and navigator locations for MR coronary angiography. *AJR Am J Roentgenol* 1997;168:1369-1375.
  62. Wang Y, Rossman PJ, Grimm RC, Riederer SJ, Ehman RL. Navigator-echo-based real-time respiratory gating and triggering for reduction of respiration effects in three-dimensional coronary MR angiography. *Radiology* 1996;198:55-60.
  63. Baltes C, Kozerke S, Atkinson D, Boesiger P. Retrospective respiratory motion correction for navigated cine velocity mapping. *J Cardiovasc Magn Reson* 2004;6:785-792.
  64. Bailes DR, Gilderdale DJ, Bydder GM, Collins AG, Firmin DN. Respiratory ordered phase encoding (ROPE): a method for reducing respiratory motion artefacts in MR imaging. *J Comput Assist Tomogr* 1985;9:835-838.
  65. Felmlee JP, Ehman RL, Riederer SJ, Korin HW. Adaptive motion compensation in MRI: accuracy of motion measurement. *Magn Reson Med* 1991;18:207-213.
  66. Wang Y, Riederer SJ, Ehman RL. Respiratory motion of the heart: kinematics and the implications for the spatial resolution in coronary imaging. *Magn Reson Med* 1995;33:713-719.
  67. Nehrke K, Bornert P, Manke D, Bock JC. Free-breathing cardiac MR imaging: study of implications of respiratory motion—initial results. *Radiology* 2001;220:810-815.
  68. Buehrer M, Curcic J, Boesiger P, Kozerke S. Prospective self-gating for simultaneous compensation of cardiac and respiratory motion. *Magn Reson Med* 2008;60:683-690.
  69. Uribe S, Muthurangu V, Boubertakh R, et al. Whole-heart cine MRI using real-time respiratory self-gating. *Magn Reson Med* 2007;57:606-613.
  70. Uribe S, Beerbaum P, Sorensen TS, Rasmusson A, Razavi R, Schaeffter T. Four-dimensional (4D) flow of the whole heart and great vessels using real-time respiratory self-gating. *Magn Reson Med* 2009;62:984-992.
  71. Winkelmann S, Schaeffter T, Koehler T, Eggers H, Doessel O. An optimal radial profile order based on the Golden Ratio for time-resolved MRI. *IEEE Trans Med Imaging* 2007;26:68-76.
  72. Batchelor PG, Atkinson D, Irrazaval P, Hill DL, Hajnal J, Larkman D. Matrix description of general motion correction applied to multishot images. *Magn Reson Med* 2005;54:1273-1280.
  73. Odille F, Vuissoz PA, Marie PY, Felblinger J. Generalized reconstruction by inversion of coupled systems (GRICS) applied to free-breathing MRI. *Magn Reson Med* 2008;60:146-157.
  74. Walker PG, Cranney GB, Scheidegger MB, Waseleski G, Pohost GM, Yoganathan AP. Semiautomated method for noise reduction and background phase error correction in MR phase velocity data. *J Magn Reson Imaging* 1993;3:521-530.
  75. Bernstein MA, Zhou XJ, Polzin JA, et al. Concomitant gradient terms in phase contrast MR: analysis and correction. *Magn Reson Med* 1998;39:300-308.
  76. Markl M, Bammer R, Alley MT, et al. Generalized reconstruction of phase contrast MRI: analysis and correction of the effect of gradient field distortions. *Magn Reson Med* 2003;50:791-801.
  77. Thomsen HS, Morcos SK, Dawson P. Is there a causal relation between the administration of gadolinium-based contrast media and the development of nephrogenic systemic fibrosis (NSF)? *Clin Radiol* 2006;61:905-906.
  78. Bernstein MA, Ikezaki Y. Comparison of phase-difference and complex-difference processing in phase-contrast MR angiography. *J Magn Reson Imaging* 1991;1:725-729.
  79. Napel S, Lee DH, Frayne R, Rutt BK. Visualizing three-dimensional flow with simulated streamlines and three-dimensional phase-contrast MR imaging. *J Magn Reson Imaging* 1992;2:143-153.
  80. Markl M, Draney MT, Hope MD, et al. Time-resolved 3-dimensional velocity mapping in the thoracic aorta: visualization of 3-directional blood flow patterns in healthy volunteers and patients. *J Comput Assist Tomogr* 2004;28:459-468.
  81. Kilner PJ, Yang GZ, Mohiaddin RH, Firmin DN, Longmore DB. Helical and retrograde secondary flow patterns in the aortic arch studied by three-directional magnetic resonance velocity mapping. *Circulation* 1993;88(5 Pt 1):2235-2247.
  82. Frydrychowicz A, Arnold R, Harloff A, et al. In vivo 3-dimensional flow connectivity mapping after extracardiac total cavopulmonary connection. *Circulation* 2008;118:e16-17.
  83. Nordmeyer S, Riesenkampff E, Crelier G, et al. Flow-sensitive four-dimensional cine magnetic resonance imaging for offline blood flow quantification in multiple vessels: a validation study. *J Magn Reson Imaging* 2010;32:677-683.
  84. Markl M, Wegent F, Zech T, et al. In vivo wall shear stress distribution in the carotid artery: effect of bifurcation geometry, internal carotid artery stenosis, and recanalization therapy. *Circ Cardiovasc Imaging* 2010;3:647-655.
  85. Oshinski JN, Curtin JL, Loth F. Mean-average wall shear stress measurements in the common carotid artery. *J Cardiovasc Magn Reson* 2006;8:717-722.
  86. Harloff A, Nussbaumer A, Bauer S, et al. In vivo assessment of wall shear stress in the atherosclerotic aorta using flow-sensitive 4D MRI. *Magn Reson Med* 2010;63:1529-1536.
  87. Stadlbauer A, van der Riet W, Crelier G, Salomonowitz E. Accelerated time-resolved three-dimensional MR velocity mapping of blood flow patterns in the aorta using SENSE and k-t BLAST. *Eur J Radiol* 2010;75:e15-21.
  88. Klipstein RH, Firmin DN, Underwood SR, Rees RS, Longmore DB. Blood flow patterns in the human aorta studied by magnetic resonance. *Br Heart J* 1987;58:316-323.
  89. Frydrychowicz A, Markl M, Hirtler D, et al. Aortic hemodynamics in patients with and without repair of aortic coarctation: in vivo analysis by 4D flow-sensitive magnetic resonance imaging. *Invest Radiol* 2011;46:317-325.
  90. Hope MD, Hope TA, Urbania TH, Higgins CB. Four-dimensional flow magnetic resonance imaging with wall shear stress analysis before and after repair of aortopulmonary fistula. *Circ Cardiovasc Imaging* 2010;3:766-768.
  91. Hope MD, Meadows AK, Hope TA, et al. Clinical evaluation of aortic coarctation with 4D flow MR imaging. *J Magn Reson Imaging* 2010;31:711-718.
  92. Crook SES, Hope TA. Arch hypoplasia and aneurysm after aortic coarctation repair: Abnormal flow may be the link. *JACC Cardiovascular Imaging* 2011;4:685-686.
  93. Frydrychowicz A, Arnold R, Hirtler D, et al. Multidirectional flow analysis by cardiovascular magnetic resonance in aneurysm development following repair of aortic coarctation. *J Cardiovasc Magn Reson* 2008;10:30.
  94. Harloff A, Strecker C, Frydrychowicz AP, et al. Plaques in the descending aorta: a new risk factor for stroke? Visualization of potential embolization pathways by 4D MRI. *J Magn Reson Imaging* 2007;26:1651-1655.
  95. Hope MD, Hope TA, Meadows AK, et al. Bicuspid aortic valve: four-dimensional MR evaluation of ascending aortic systolic flow patterns. *Radiology* 2010;255:53-61.
  96. Hope MD, Meadows AK, Hope TA, et al. Images in cardiovascular medicine. Evaluation of bicuspid aortic valve and aortic coarctation with 4D flow magnetic resonance imaging. *Circulation* 2008;117:2818-2819.
  97. Barker AJ, Lanning C, Shandas R. Quantification of hemodynamic wall shear stress in patients with bicuspid aortic valve using phase-contrast MRI. *Ann Biomed Eng* 2010;38:788-800.
  98. Kvitting JP, Ebbens T, Wigstrom L, Engvall J, Olin CL, Bolger AF. Flow patterns in the aortic root and the aorta studied with time-resolved, 3-dimensional, phase-contrast magnetic resonance imaging: implications for aortic valve-sparing surgery. *J Thorac Cardiovasc Surg* 2004;127:1602-1607.
  99. Markl M, Draney MT, Miller DC, et al. Time-resolved three-dimensional magnetic resonance velocity mapping of aortic flow in healthy volunteers and patients after valve-sparing aortic root replacement. *J Thorac Cardiovasc Surg* 2005;130:456-463.

100. Carabello BA, Paulus WJ. Aortic stenosis. *Lancet* 2009;373:956–966.
101. Wilton E, Jahangiri M. Post-stenotic aortic dilatation. *J Cardiothorac Surg* 2006;1:7.
102. Barker AJ, Markl M. Editorial. The role of hemodynamics in bicuspid aortic valve disease. *Eur J Cardiothorac Surg* 2011;39:805–806.
103. Sigovan M, Hope MD, Dyverfeldt P, Saloner D. Comparison of 4D flow parameters for quantification of flow eccentricity in the ascending aorta. *J Magn Reson Imaging* 2011;34:1226–1230.
104. Hope MD, Hope TA, Crook SES, et al. 4-dimensional flow cardiac magnetic resonance in assessment of valve-related ascending aortic disease. *JACC Cardiovascular Imaging* 2011;4:781–787.
105. den Reijer PM, Sallee D 3rd, van der Velden P, et al. Hemodynamic predictors of aortic dilatation in bicuspid aortic valve by velocity-encoded cardiovascular magnetic resonance. *J Cardiovasc Magn Reson* 2010;12:4.
106. Amarencu P, Cohen A, Tzourio C, et al. Atherosclerotic disease of the aortic arch and the risk of ischemic stroke. *N Engl J Med* 1994;331:1474–1479.
107. Sen S, Hinderliter A, Sen PK, et al. Aortic arch atheroma progression and recurrent vascular events in patients with stroke or transient ischemic attack. *Circulation* 2007;116:928–935.
108. Kronzon I, Tunick PA. Aortic atherosclerotic disease and stroke. *Circulation* 2006;114:63–75.
109. Reimold SC, Maier SE, Aggarwal K, et al. Aortic flow velocity patterns in chronic aortic regurgitation: implications for Doppler echocardiography. *J Am Soc Echocardiogr* 1996;9:675–683.
110. Svedlund S, Wetterholm R, Volkmann R, Caidahl K. Retrograde blood flow in the aortic arch determined by transesophageal Doppler ultrasound. *Cerebrovasc Dis* 2009;27:22–28.
111. Bogren HG, Buonocore MH, Valente RJ. Four-dimensional magnetic resonance velocity mapping of blood flow patterns in the aorta in patients with atherosclerotic coronary artery disease compared to age-matched normal subjects. *J Magn Reson Imaging* 2004;19:417–427.
112. Harloff A, Simon J, Brendecke S, et al. Complex plaques in the proximal descending aorta: an underestimated embolic source of stroke. *Stroke* 2010;41:1145–1150.
113. Harloff A, Strecker C, Dudler P, et al. Retrograde embolism from the descending aorta: visualization by multidirectional 3D velocity mapping in cryptogenic stroke. *Stroke* 2009;40:1505–1508.
114. Markl M, Geiger J, Kilner PJ, et al. Time-resolved three-dimensional magnetic resonance velocity mapping of cardiovascular flow paths in volunteers and patients with Fontan circulation. *Eur J Cardiothorac Surg* 2011;39:206–212.
115. Sanz J, Kuschner P, Rius T, et al. Pulmonary arterial hypertension: noninvasive detection with phase-contrast MR imaging. *Radiology* 2007;243:70–79.
116. Kircher BJ, Himelman RB, Schiller NB. Noninvasive estimation of right atrial pressure from the inspiratory collapse of the inferior vena cava. *Am J Cardiol* 1990;66:493–496.
117. Nogami M, Ohno Y, Koyama H, et al. Utility of phase contrast MR imaging for assessment of pulmonary flow and pressure estimation in patients with pulmonary hypertension: comparison with right heart catheterization and echocardiography. *J Magn Reson Imaging* 2009;30:973–980.
118. Yang GZ, Kilner PJ, Wood NB, Underwood SR, Firmin DN. Computation of flow pressure fields from magnetic resonance velocity mapping. *Magn Reson Med* 1996;36:520–526.
119. Bley TA, Johnson KM, Wieben O, et al. Non-invasive assessment of transstenotic pressure gradients utilizing 3D phase contrast MR: validation against endovascular pressure measurements in a porcine study. In: *Proc 17th Annual Meeting ISMRM, Honolulu*; 2009:425.
120. Reiter G, Reiter U, Kovacs G, et al. Magnetic resonance-derived 3-dimensional blood flow patterns in the main pulmonary artery as a marker of pulmonary hypertension and a measure of elevated mean pulmonary arterial pressure. *Circ Cardiovasc Imaging* 2008;1:23–30.
121. Helderma F, Mauritz GJ, Andringa KE, Vonk-Noordegraaf A, Marcus JT. Early onset of retrograde flow in the main pulmonary artery is a characteristic of pulmonary arterial hypertension. *J Magn Reson Imaging* 2011;33:1362–1368.
122. Markl M, Kilner PJ, Ebbers T. Comprehensive 4D velocity mapping of the heart and great vessels by cardiovascular magnetic resonance. *J Cardiovasc Magn Reson* 2011;13:7.
123. Kim WY, Walker PG, Pedersen EM, et al. Left ventricular blood flow patterns in normal subjects: a quantitative analysis by three-dimensional magnetic resonance velocity mapping. *J Am Coll Cardiol* 1995;26:224–238.
124. Eriksson J, Carlhall CJ, Dyverfeldt P, Engvall J, Bolger AF, Ebbers T. Semi-automatic quantification of 4D left ventricular blood flow. *J Cardiovasc Magn Reson* 2010;12:9.
125. Bolger AF, Heiberg E, Karlsson M, et al. Transit of blood flow through the human left ventricle mapped by cardiovascular magnetic resonance. *J Cardiovasc Magn Reson* 2007;9:741–747.
126. Carlhall CJ, Bolger A. Passing strange: flow in the failing ventricle. *Circ Heart Fail* 2010;3:326–331.
127. Westenberg JJ, Roes SD, Ajmone Marsan N, et al. Mitral valve and tricuspid valve blood flow: accurate quantification with 3D velocity-encoded MR imaging with retrospective valve tracking. *Radiology* 2008;249:792–800.
128. Toger J, Carlsson M, Soderlind G, Arheden H, Heiberg E. Volume Tracking: A new method for quantitative assessment and visualization of intracardiac blood flow from three-dimensional, time-resolved, three-component magnetic resonance velocity mapping. *BMC Med Imaging* 2011;11:10.
129. Geiger J, Markl M, Jung B, et al. 4D-MR flow analysis in patients after repair for tetralogy of Fallot. *Eur Radiol* 2011;21:1651–1657.
130. Nanashima A, Shibasaki S, Sakamoto I, et al. Clinical evaluation of magnetic resonance imaging flowmetry of portal and hepatic veins in patients following hepatectomy. *Liver Int* 2006;26:587–594.
131. Applegate GR, Thaete FL, Meyers SP, et al. Blood flow in the portal vein: velocity quantitation with phase-contrast MR angiography. *Radiology* 1993;187:253–256.
132. Burkart DJ, Johnson CD, Morton MJ, Wolf RL, Ehman RL. Volumetric flow rates in the portal venous system: measurement with cine phase-contrast MR imaging. *AJR Am J Roentgenol* 1993;160:1113–1118.
133. Dumoulin CL, Yucel EK, Vock P, et al. Two- and three-dimensional phase contrast MR angiography of the abdomen. *J Comput Assist Tomogr* 1990;14:779–784.
134. Kashitani N, Kimoto S, Tsunoda M, et al. Portal blood flow in the presence or absence of diffuse liver disease: measurement by phase contrast MR imaging. *Abdom Imaging* 1995;20:197–200.
135. Nghiem HV, Winter TC 3rd, Mountford MC, et al. Evaluation of the portal venous system before liver transplantation: value of phase-contrast MR angiography. *AJR Am J Roentgenol* 1995;164:871–878.
136. Sugano S, Yamamoto K, Sasao K, Watanabe M. Portal venous blood flow while breath-holding after inspiration or expiration and during normal respiration in controls and cirrhotics. *J Gastroenterol* 1999;34:613–618.
137. Nakano S, Katoh T, Ohki M, et al. Pharmacologically stimulated portal flow measurement by magnetic resonance imaging for assessment of liver function. *Radiat Med* 1999;17:21–26.
138. Stankovic Z, Frydrychowicz A, Csatar Z, et al. MR-based visualization and quantification of three-dimensional flow characteristics in the portal venous system. *J Magn Reson Imaging* 2010;32:466–475.
139. Stankovic Z, Csatar Z, Deibert P, et al. Time-resolved qualitative and quantitative analysis of normal and altered 3D portal venous hemodynamics in liver cirrhosis patients. *Radiology* 2012, in press.
140. Lee AT, Pike GB, Pelc NJ. Three-point phase-contrast velocity measurements with increased velocity-to-noise ratio. *Magn Reson Med* 1995;33:122–126.
141. Nett EJ, Frydrychowicz A, Johnson KM, Schrauben E, Francois CJ, Wieben O. Accelerated dual Venc phase contrast VIPR in healthy volunteers. In: *Proc 19th Annual Meeting ISMRM, Montreal*; 2011:1222.
142. Missouri CG, Buckenham T, Cappuccio FP, MacGregor GA. Renal artery stenosis: a common and important problem in patients with peripheral vascular disease. *Am J Med* 1994;96:10–14.
143. Gross CM, Kramer J, Weingartner O, et al. Determination of renal arterial stenosis severity: comparison of pressure gradient and vessel diameter. *Radiology* 2001;220:751–756.

144. Agarwal R, Brunelli SM, Williams K, Mitchell MD, Feldman HI, Umscheid CA. Gadolinium-based contrast agents and nephrogenic systemic fibrosis: a systematic review and meta-analysis. *Nephrol Dial Transplant* 2009;24:856–863.
145. Schoenberg SO, Knopp MV, Bock M, et al. Renal artery stenosis: grading of hemodynamic changes with cine phase-contrast MR blood flow measurements. *Radiology* 1997;203:45–53.
146. Prince MR, Schoenberg SO, Ward JS, Londy FJ, Wakefield TW, Stanley JC. Hemodynamically significant atherosclerotic renal artery stenosis: MR angiographic features. *Radiology* 1997;205:128–136.
147. Harloff A, Albrecht F, Spreer J, et al. 3D blood flow characteristics in the carotid artery bifurcation assessed by flow-sensitive 4D MRI at 3T. *Magn Reson Med* 2009;61:65–74.
148. Lee SW, Antiga L, Spence JD, Steinman DA. Geometry of the carotid bifurcation predicts its exposure to disturbed flow. *Stroke* 2008;39:2341–2347.
149. Malek AM, Alper SL, Izumo S. Hemodynamic shear stress and its role in atherosclerosis. *JAMA* 1999;282:2035–2042.
150. Cheng C, Tempel D, van Haperen R, et al. Atherosclerotic lesion size and vulnerability are determined by patterns of fluid shear stress. *Circulation* 2006;113:2744–2753.
151. Bammer R, Hope TA, Aksoy M, Alley MT. Time-resolved 3D quantitative flow MRI of the major intracranial vessels: initial experience and comparative evaluation at 1.5T and 3.0T in combination with parallel imaging. *Magn Reson Med* 2007;57:127–140.
152. Wetzel S, Meckel S, Frydrychowicz A, et al. In vivo assessment and visualization of intracranial arterial hemodynamics with flow-sensitized 4D MR imaging at 3T. *AJNR Am J Neuroradiol* 2007;28:433–438.
153. Yamashita S, Isoda H, Hirano M, et al. Visualization of hemodynamics in intracranial arteries using time-resolved three-dimensional phase-contrast MRI. *J Magn Reson Imaging* 2007;25:473–478.
154. Meckel S, Stalder AF, Santini F, et al. In vivo visualization and analysis of 3-D hemodynamics in cerebral aneurysms with flow-sensitized 4-D MR imaging at 3 T. *Neuroradiology* 2008;50:473–484.
155. Rayz VL, Boussel L, Ge L, et al. Flow residence time and regions of intraluminal thrombus deposition in intracranial aneurysms. *Ann Biomed Eng* 2010;38:3058–3069.
156. Hope TA, Hope MD, Purcell DD, et al. Evaluation of intracranial stenoses and aneurysms with accelerated 4D flow. *Magn Reson Imaging* 2010;28:41–46.
157. Boussel L, Rayz V, Martin A, et al. Phase-contrast magnetic resonance imaging measurements in intracranial aneurysms in vivo of flow patterns, velocity fields, and wall shear stress: comparison with computational fluid dynamics. *Magn Reson Med* 2009;61:409–417.
158. Isoda H, Ohkura Y, Kosugi T, et al. In vivo hemodynamic analysis of intracranial aneurysms obtained by magnetic resonance fluid dynamics (MRFD) based on time-resolved three-dimensional phase-contrast MRI. *Neuroradiology* 2010;52:921–928.
159. Boussel L, Rayz V, McCulloch C, et al. Aneurysm growth occurs at region of low wall shear stress: patient-specific correlation of hemodynamics and growth in a longitudinal study. *Stroke* 2008;39:2997–3002.
160. Goyen M, Heuser LJ. Improved peripheral MRA using multi-velocity-encoding phase contrast-enhanced MRA techniques. *Acta Radiol* 2000;41:139–141.
161. Steffens JC, Link J, Muller-Hulsbeck S, Freund M, Brinkmann G, Heller M. Cardiac-gated two-dimensional phase-contrast MR angiography of lower extremity occlusive disease. *AJR Am J Roentgenol* 1997;169:749–754.
162. Swan JS, Grist TM, Weber DM, Sproat IA, Wojtowycz MM. MR angiography of the pelvis with variable velocity encoding and a phased-array coil. *Radiology* 1994;190:363–369.
163. Yucel EK, Dumoulin CL, Waltman AC. MR angiography of lower-extremity arterial disease: preliminary experience. *J Magn Reson Imaging* 1992;2:303–309.
164. Krug B, Kugel H, Friedmann G, et al. MR imaging of poststenotic flow phenomena: experimental studies. *J Magn Reson Imaging* 1991;1:585–591.
165. Krug B, Kugel H, Harnischmacher U, Heindel W, Schmidt R, Krings F. MR pulsatility measurements in peripheral arteries: preliminary results. *Magn Reson Med* 1995;34:698–705.
166. Mohajer K, Zhang H, Gurell D, et al. Superficial femoral artery occlusive disease severity correlates with MR cine phase-contrast flow measurements. *J Magn Reson Imaging* 2006;23:355–360.
167. Pena CS, McCauley TR, Price TB, Sumpio B, Gusberg RJ, Gore JC. Quantitative blood flow measurements with cine phase-contrast MR imaging of subjects at rest and after exercise to assess peripheral vascular disease. *AJR Am J Roentgenol* 1996;167:153–157.
168. Frydrychowicz A, Winterer JT, Zaitsev M, et al. Visualization of iliac and proximal femoral artery hemodynamics using time-resolved 3D phase contrast MRI at 3T. *J Magn Reson Imaging* 2007;25:1085–1092.
169. Prince MR. Is there replacement for percentage stenosis in characterizing occlusive vascular disease? *Radiology* 2007;245:617–618.
170. Tsao J, Boesiger P, Pruessmann KP. k-t BLAST and k-t SENSE: dynamic MRI with high frame rate exploiting spatiotemporal correlations. *Magn Reson Med* 2003;50:1031–1042.
171. Lustig M, Donoho D, Pauly JM. Sparse MRI: the application of compressed sensing for rapid MR imaging. *Magn Reson Med* 2007;58:1182–1195.
172. Bock J, Frydrychowicz A, Stalder AF, et al. 4D phase contrast MRI at 3 T: effect of standard and blood-pool contrast agents on SNR, PC-MRA, and blood flow visualization. *Magn Reson Med* 2010;63:330–338.